Bioactive Materials 6 (2021) 2039–2057

Contents lists available at ScienceDirect

Bioactive Materials

journal homepage: www.sciencedirect.com/journal/bioactive-materials

Phosphorylation inhibition of protein-tyrosine phosphatase 1B tyrosine-152 induces bone regeneration coupled with angiogenesis for bone tissue engineering

Yong Tang [a,d,e,2], Keyu Luo [a,c,2], Yin Chen [d,2], Yueqi Chen [a,b], Rui Zhou [a], Can Chen [a], Jiulin Tan [a], Moyuan Deng [a], Qijie Dai [a], Xueke Yu [a], Jian Liu [a], Chengmin Zhang [a], Wenjie Wu [a], Jianzhong Xu [a,**,1], Shiwu Dong [a,b,***,1], Fei Luo [a,*,1]

[a] National & Regional United Engineering Lab of Tissue Engineering, Department of Orthopedics, Southwest Hospital, Third Military Medical University, Chongqing, China
[b] Department of Biomedical Materials Science, Third Military Medical University, Chongqing, China
[c] Department of Spine Surgery, Center for Orthopedics, Daping Hospital, Third Military Medical University, Chongqing, China
[d] State Key Laboratory of Trauma, Burns and Combined Injury, Institute of Combined Injury, Chongqing Engineering Research Center for Nanomedicine, College of Preventive Medicine, Third Military Medical University, Chongqing, China
[e] Department of Orthopaedics, 72nd Group Army Hospital, Huzhou University, Huzhou, Zhejiang, China

ARTICLE INFO

Keywords:
PTP1B
Bone regeneration
Angiogenesis
Cell migration
Type H vessels

ABSTRACT

A close relationship has been reported to exist between cadherin-mediated cell–cell adhesion and integrin-mediated cell mobility, and protein tyrosine phosphatase 1B (PTP1B) may be involved in maintaining this homeostasis. The stable residence of mesenchymal stem cells (MSCs) and endothelial cells (ECs) in their niches is closely related to the regulation of PTP1B. However, the exact role of the departure of MSCs and ECs from their niches during bone regeneration is largely unknown. Here, we show that the phosphorylation state of PTP1B tyrosine-152 (Y152) plays a central role in initiating the departure of these cells from their niches and their subsequent recruitment to bone defects. Based on our previous design of a PTP1B Y152 region-mimicking peptide (152RM) that significantly inhibits the phosphorylation of PTP1B Y152, further investigations revealed that 152RM enhanced cell migration partly via integrin αvβ3 and promoted MSCs osteogenic differentiation partly by inhibiting ATF3. Moreover, 152RM induced type H vessels formation by activating Notch signaling. Demineralized bone matrix (DBM) scaffolds were fabricated with mesoporous silica nanoparticles (MSNs), and 152RM was then loaded onto them by electrostatic adsorption. The DBM-MSN/152RM scaffolds were demonstrated to induce bone formation and type H vessels expansion *in vivo*. In conclusion, our data reveal that 152RM contributes to bone formation by coupling osteogenesis with angiogenesis, which may offer a potential therapeutic strategy for bone defects.

1. Introduction

The repair of bone defects caused by severe trauma, infection or tumor resection is a common and important orthopedic challenge in the clinic [1]. Bone marrow mesenchymal stem cells (MSCs) and endothelial cells (ECs) play key roles in bone repair. Recruitment of a sufficient number of MSCs and ECs from the bone marrow and periosteum of adjacent tissues to the bone defect area is required for bone repair [2]. MSCs mainly reside in the bone marrow pool and periosteum under physiological conditions, and they live in a particular microenvironment called stem cell niches [3]. Most MSCs and osteoblast progenitor cells

Peer review under responsibility of KeAi Communications Co., Ltd.
* Corresponding author. , Southwest Hospital, Third Military Medical University, No 30, Gaotanyan Street, Shapingba, Chongqing, 400038, China.
** Corresponding author. , Southwest Hospital, Third Military Medical University, No 30, Gaotanyan Street, Shapingba, Chongqing, 400038, China.
*** Corresponding author. , Department of Biomedical Materials Science, Third Military Medical University, No 30, Gaotanyan Street, Shapingba, Chongqing, 400038, China.
E-mail addresses: xujzspine@126.com (J. Xu), dongshiwu@tmmu.edu.cn (S. Dong), luofly1009@hotmail.com (F. Luo).
[1] Jianzhong Xu, Shiwu Dong and Fei Luo contributed equally to this work and should be considered as Corresponding authors.
[2] Yong Tang, Keyu Luo and Yin Chen contributed equally to this work and should be considered as first authors.

https://doi.org/10.1016/j.bioactmat.2020.12.025
Received 4 October 2020; Received in revised form 6 December 2020; Accepted 25 December 2020

Abbreviations

PTP1B	protein tyrosine phosphatase 1B
MSCs	marrow mesenchymal stem cells
Y152	tyrosine-152
DBM	Demineralized bone matrix
152RM	PTP1B Y152 region mimicking peptide;
ECs	endothelial cells
DBM	Demineralized bone matrix
MSNs	mesoporous silica nanoparticles
BET	Brunauer-Emmett–Teller
CCK-8	Cell Counting Kit-8
micro-CT	Micro-computed tomography
3D	Three-dimensional
ATF3	activation transcription factor 3
ER	endoplasmic reticulum
FAK	focal adhesion kinase
MAR	mineral apposition rate
BFR/BS	bone formation rate per bone surface
BMD	bone mineral density
BV/TV	trabecular bone volume fraction
Tb.N:	trabecular number
Tb.Th	trabecular thickness
Tb.Sp:	trabecular separation
MAR	mineral apposition rate
BFR/BS	bone formation rate per bone surface
RNA-seq	RNA-sequencing
SEM	scanning electron microscopy
TEM	Transmission electron microscopy
TGA	thermogravimetric analysis
OPN	osteopontin
Runx2	runt-related transcription factor 2
OCN	osteocalcin

are very prominent around vessels [4]. Therefore, ECs are important for maintaining MSC niches. The departure of MSCs from their niches to initiate recruitment is the first step of bone repair. This process involves initiation of the transformation from cadherin-mediated cell–cell adhesion to integrin-dependent cell migration [5,6]. Multiple cytokines and hypoxia can recruit MSCs and ECs to bone defects [7]. However, these factors have not been applied effectively, and this approach is still limited to the experimental stage. Due to disadvantages associated with cytokines, such as their low synthetic activity and vulnerability to degradation, it is difficult to develop bioactive materials to activate the recruitment of MSCs and ECs from their niches to bone defects.

Protein tyrosine phosphatase 1B (PTP1B) is a nonreceptor tyrosine phosphatase that exists primarily in an endoplasmic reticulum-anchored form [8]. PTP1B plays a dual regulatory role in cadherin- and integrin-related pathways. PTP1B inhibitors can decrease the adhesion between MSCs within their niche cells but inhibit their migration [9]. Conversely, PTP1B inhibitors can induce ECs motility [10]. Tyrosine-152 (Y152) phosphorylation of PTP1B is critical for stabilization of the cadherin and β-catenin adhesion complex, which is key to enhancing cell–cell adhesion and decreasing cell migration [11]. However, there is no specific inhibitor targeting PTP1B Y152.

We previously designed a PTP1B Y152 region-mimicking peptide (152RM) and verified that it could effectively inhibit PTP1B Y152 phosphorylation [12]. Our results demonstrated that 152RM promotes the disintegration of the cadherin and β-catenin adhesion complex, inhibits cadherin-mediated cell–cell adhesion and enhances integrin-mediated migration [12]. Therefore, we attempted to further verify these effects *in vivo*. 152RM is essentially a polypeptide that needs to be released stably under the control of appropriate scaffolds. Under acidic conditions in bone defects, collagen matrix formation is thought to precede mineralization [13]. Demineralized bone matrix (DBM) is a porous bone bioactive scaffold that is composed of collagen I and has cell adhesion and osteogenesis induction capacity [14]. To increase the drug-loading capacity of the scaffolds, we chose mesoporous silica nanoparticles (MSNs) to construct the carrier. MSNs have excellent morphological and physicochemical properties, which allow them to serve as the basis of carrier applications [15]. MSNs have good biocompatibility, high drug-loading capacity and good drug release performance. Their mesoporous structure has a good protective effect against peptide drugs [16].

Here, we modified the surface of DBM scaffolds with MSNs and then loaded 152RM by electrostatic adsorption. The DBM-MSN/152RM scaffolds were assessed in terms of cell migration, differentiation, osteogenic induction capacity, vascularization, and bone regeneration coupled with angiogenesis *in vivo*. Our data demonstrate that DBM-MSN/152RM scaffolds exert a therapeutic effect on bone defects by recruiting MSCs and ECs from their niches to bone defects, providing a new option for the treatment of bone repair disorders in patients.

2. Materials and methods

2.1. Animals

One hundred SD rats were purchased from Biocytogen Co., Ltd. (Beijing, China). For dynamic histomorphometric analysis, rats were separately injected with xylenol orange (90 mg/kg) and calcein (30 mg/kg) 10 days and 3 days before sacrifice, respectively. The rat femur defect model was established as previously described [7]. A bicortical channel was widened gradually to a diameter of 3.5 mm with a slow-speed electric drill. After the bone was removed, the drilled holes were rinsed with saline solution, and the scaffolds were implanted into the defects. All rats were treated following the guidelines of the committee on animal care (Third Military Medical University).

2.2. Preparation of MSCs and ECs

Primary MSCs were isolated according to previously published methods [17]. For MSC preparation, $CD45^{-}Ter119^{-}$ cells were obtained from compact mouse bone with an MSC enrichment kit (Stem Cell Technologies, Vancouver, BC, Canada). Then, the cells were grown in a MesenCult™ Osteogenic Stimulatory Kit (Mouse) (Stem Cell Technologies). Primary ECs were purchased from Shanghai Zhong Qiao Xin Zhou Biotechnology Co., Ltd. (ZQ0446; Shanghai, China). All experiments were performed on fresh, low-passage (p2-3) cells.

2.3. Fabrication of DBM-MSN/152RM scaffolds

The PTP1B Y152 region-mimicking peptide (152RM; desalted, purity >98%) was commercially synthesized and authenticated (China Peptides Co., Ltd., Shanghai, China). The peptide sequence is "ISEDIKSYYTVRQLE-YGRKKRRQRRR". MSNs were manufactured as previously described [18]. The demineralized bone matrix (DBM) scaffolds were purchased from Datsing Biotech Co., Ltd. (Beijing, China). DBM was first immersed in the 70% ethanol solution for 2 h to remove impurities on its surface. Then, the scaffolds were rinsed with water and dried in a vacuum oven. Next, they were dispersed in ultrapure water (100 mL). Then, EDC (55 mg), NHS (32.5 mg) and 2 mg of MSNs were added to the solution and stirred for another 16 h at 4 °C. These DBM-MSNs were washed with ultrapure water three times and dried in a freeze dryer. Then, they were placed into 1 mg/mL 152RM PBS solution

for another 12 h, cleaned with water, dried with nitrogen, and assembled. The DBM-MSN/152RM scaffolds were fabricated. During the manufacturing process, a total of four scaffolds were fabricated for further analysis: pure DBM scaffolds, DBM-MSN scaffolds, DBM/152RM scaffolds and DBM-MSN/152RM scaffolds. All the scaffolds were sterilized via gamma irradiation before the cell and animal experiments.

2.4. Characterization of the scaffolds

The size, zeta potential, morphology and elemental maps were determined as previously described [19]. The material morphology, energy dispersive X-ray spectroscopy (EDS), and corresponding EDS mapping element maps were visualized by TEM (Tecnai G2 F20 U-TWIN, FEI, Hillsboro, OR, US) (ESEM, Quanta 200, FEI). Thermogravimetric analysis (TGA) was performed on a DTG-60AH thermogravimetric analyzer (Shimadzu, Japan). The zeta potential and size distribution were measured with a Nano-ZS (Malvern, Worcestershire, UK) at room temperature. Nitrogen adsorption-desorption isotherms were obtained on a Micromeritics Tristar 3000 pore analyzer (Micromeritics, Norcross, GA, US). Brunauer-Emmett–Teller (BET) analysis was used to calculate the surface area and pore size.

The average pore size was measured by the average of the transverse minimum and maximum diameters of each hole (10 holes per sample).

2.5. Detection of peptide release in vitro

The 152RM loading efficiency and loading percentage and the amount of 152RM released were determined as previously described [20]. DBM-MSN/152RM and DBM/152RM at a peptide concentration of 1 mg/mL were prepared in 1 mL of phosphate buffer (pH = 6.8) and stirred at 37 °C. The supernatant was obtained via high-speed centrifugation (5000 g) after 2 h, and the precipitate was resuspended in 1 mL of phosphate buffer. Similarly, the supernatant was collected at 6, 12, 24, 48, 72, 96, 120, 144, 168, and 192 h post-initial dissolution. The content of 152RM was determined by the BCA method to standardize the data (Beyotime, Haimen, China).

2.6. Cell biocompatibility measurements in vitro

The viability of cells on the scaffolds was analyzed by a live/dead cell staining kit (Dojindo, Japan). After a 24 h coculture, cells attached to the specimens were stained with 500 μL of combination dye for 10 min in the incubator and were then subjected to fluorescence microscopy (LSM780; Carl Zeiss, Germany). At the designated time points (1, 4, and 7 days), the cells were labeled with 5 μg/mL Alexa Fluor 594 phalloidin (Life Tech, US) for 15 min and 4,6-diamidino-2-phenylindole dilactate (DAPI, Life Tech, US) for 5 min. The labeled cells on the scaffolds were observed by laser scanning confocal microscopy (LSM780, ZEISS). High-resolution imaging of Z-stacks was obtained, and confocal Z-stacks of images were processed. Cell cytotoxicity was analyzed with Cell Counting Kit-8 (CCK-8) assays (Dojindo Kagaku, Japan). The solution absorbance was measured at a wavelength of 450 nm with an M2e microplate reader (Molecular Devices, Silicon Valley, CA, US).

2.7. In vitro assays of the migration of MSCs and ECs

We assessed cell migration in 12-well Transwell plates (Corning Inc.) with filters with 8-μm pores. In brief, we seeded 1×10^4/well MSCs or ECs in the upper chambers and preincubated them with vehicle, 20 μM Cyclo(-RGDfK) (an integrin αvβ3 inhibitor; MedChemExpress), 20 μM AMD 3100 (a CXCR4 inhibitor; MedChemExpress), 20 μM ATN-161 (an integrin α5β1 inhibitor; Selleck Chem), 1 μM J-113863 (a CCR1 inhibitor; MedChemExpress), 1 μM CCR3 antagonist 1 (a CCR3 inhibitor; MedChemExpress), 1 μM TAK-220 (a CCR5 inhibitor; MedChemExpress), 20 μM Ki8751 (a VEGFR2 inhibitor; MedChemExpress), 10 μM SB225002 (a CXCR2 inhibitor; MedChemExpress) or 2 μM Y15 (a FAK inhibitor; Sigma-Aldrich) for 1 h. Then, we incubated them with medium in the lower chambers for an additional 24 h with the inhibitor or vehicle remaining in the upper chambers. At the end of incubation, the cells were fixed with 10% formaldehyde for 30 min. The cells on the lower surface were stained with crystal violet (Sigma-Aldrich) and quantified by counting five random fields per well using a microscope (Olympus) at 200 × magnification.

2.8. Scratch assay of MSCs and ECs in vitro

A cell scratch assay was performed as previously described [21]. In brief, after the cells reached 90% confluence, a line approximately 2–3 mm wide was generated with a sterile pipet tip perpendicular to the bottom of the 6-well plate. The floating cells were rinsed with PBS. Cell images were collected at 0 h, 6 h and 12 h. Image J software was used to measure the wound and calculate the wound healing rate.

2.9. Detection of MSC differentiation

MSCs were induced to undergo osteogenic differentiation according to our previously published methods [22]. After the MSCs reached 90% confluence, they were incubated in differentiation induction medium. Alkaline phosphatase staining and activity were measured with an alkaline phosphatase assay kit (Beyotime) 1 week later. After three weeks, Alizarin Red was used for staining and quantitative analysis of mineralization (Sigma-Aldrich).

2.10. Tube formation

ECs were induced to form tubes according to our previously published methods [22]. Matrigel matrix (Corning) was added to 24-well culture plates (289 μL per well) on ice and then incubated at 37 °C for 1 h. ECs (12×10^4 cells in 300 μL per well) were seeded on polymerized Matrigel with 5 μM 152RM. After incubation on the angiogenesis assay plate for 3 h or 6 h at 37 °C, tube formation was observed with a microscope (Olympus, Tokyo, Japan), and cumulative tube length was measured. In some assays, neutralizing antibodies against VEGF (AF-493; R&D, Minneapolis, Minnesota, USA), PDGF-BB (ab34074; Abcam), TGF-β1 (9016; R&D), TGF-β3 (20,724; R&D), FGF2 (AF-233-NA; R&D), FGF22 (MAB3867; R&D) and IgG (AB-108-C; R&D) were added to the medium.

2.11. Micro-computed tomography (micro-CT)

Microcomputed tomography (Micro-CT Skyscan 1272 system; Bruker, Belgium) with an isotropic voxel size of 8 μm was used to quantify the bone parameters of the femurs, as previously described [23]. The scanning voltage was 60 kV, the current was 165 μA, and the resolution was 8 μm per pixel. A bone defect area with a diameter of 3.5 mm was selected for quantitative analysis [24]. Trabecular bones were thresholded at 90–255 (8 bit grayscale bitmap). Reconstruction was performed with Nrecon (Ver. 1.6.10). Three-dimensional (3D) images were obtained from contoured 2D images with methods based on distance transformation of the grayscale original images (CTvox, Ver. 3.0.0). The bone parameters, including bone mineral density (BMD, g/cm^3), trabecular bone volume fraction (BV/TV, %), trabecular number (Tb.N, 1/mm), and trabecular separation (Tb.Sp, mm), were calculated with CT Analyzer (Version 1.15.4.0, Belgium).

2.12. Bone histomorphometry

The femurs were fixed, dehydrated, embedded without decalcification and sliced as previously described [25]. Undecalcified femoral sections were stained with the von Kossa method or left unstained to calculate the dynamic morphometric parameters. The mineral apposition rate (MAR) and bone formation rate per bone surface (BFR/BS)

were analyzed with a laser confocal microscope (LSM780; Carl Zeiss, Oberkochen, Germany). Decalcified femoral sections underwent HE and Masson staining for analysis of static parameters.

2.13. Angiography

Micro-CT was used to image bone vessels as previously described [26,27]. In brief, the mice were euthanized, the thoracic cavity was opened, and a needle was inserted into the left ventricle to establish an inflow tract. An outflow tract was established in the right auricle. Next, heparinized saline (40 mL, 100 U/mL), 10% neutral formalin (40 mL) and silicone rubber compound (40 mL, Microfil MV-122, Flow Tech, Massachusetts, USA) were injected. The specimens were stored at 4 °C overnight and then fixed and decalcified for approximately 30 days. Images were scanned by micro-CT, and the vascular volume and vascular surface area were calculated.

2.14. Immunostaining

Immunofluorescence was performed as previously described [28,29]. Briefly, the bone sections were incubated with individual primary antibodies against mouse CD31 (ab28364; Abcam), endomucin (V.7C7; Santa Cruz), Ki67 (AF7617; R&D), beta-catenin (8480, CST), osterix (bs-1110R; Bioss), osteocalcin (bs-0470R; Bioss), Runx2 (bs-1134R; Bioss), DLL4 (bs-6044R; Bioss), Notch1 (bs-1335R; Bioss), Noggin (bs-2975R; Bioss), CXCR4 D1S7W; Cell Signaling Technology), integrin αvβ3 (bs-1310R; Bioss), CD90 (bs-20640R; Bioss), CD105 (bs-0579R; Bioss), CD271 (bs-0161R; Bioss), OPN (bs-23258R; Bioss), and phospho-VEGFR2(bs-2674R; Bioss) overnight at 4 °C. Subsequently, the samples were incubated with fluorescence-coupled secondary antibodies for 1 h at 37 °C in the dark. Images were collected using a confocal laser microscope (LSM 780; Carl Zeiss).

2.15. Real-time quantitative PCR (qPCR)

Total RNA was isolated using TRIzol reagent (Invitrogen, Carlsbad, CA, USA). Then, RNA was used to produce complementary DNA (cDNA) using the PrimeScript RT-PCR kit (DRR014A) (TaKaRa, Tokyo, Japan). Next, qPCR was performed using SYBR Premix Ex Taq II (TaKaRa) according to the manufacturer's instructions. The primer sequences are listed in Table S1.

2.16. Western blotting

MSCs or ECs were lysed using ice-cold lysis buffer containing 1% protease inhibitors and phosphatase inhibitors (Roche Applied Science, Penzberg, Germany). Proteins were fractionated by sodium dodecyl sulfate (SDS)–polyacrylamide gel electrophoresis and then transferred to polyvinylidene difluoride (PVDF) membranes. Protein expression was detected by incubation with antibodies against CXCR4 (D1S7W; Cell Signaling Technology), phospho-VEGFR2 (bs-2674R; Bioss), integrin αvβ3 (bs-1310R; Bioss), p-FAK (bsm-52155R; Bioss), FAK (bs-20735R; Bioss), p-JAK2 (SY24-03; Novus), JAK2 (bs-23003R; Bioss), p-STAT3 (bs-1658R; Bioss), STAT3 (bsm-33218 M; Bioss), ATF3 (bs-0519R; Bioss), CHOP (bs-20669R; Bioss), p-ERK1/2 (D13.14.4E; Cell Signaling Technology), ERK1/2 (137F5; Cell Signaling Technology) or β-actin (AF0003; Beyotime).

2.17. RNA-sequencing (RNA-seq)

MSCs and ECs cultured with or without 152RM for 12 h were collected, and RNA was isolated. cDNA library construction and RNA-seq were performed at Genergy Bio (Shanghai, China). RNA-seq was performed using an Illumina HiSeq2000 system. The expression of known genes was assessed by fragments per kilobase of transcript per million fragments mapped (FPKM). All raw data were deposited in the National Center for Biotechnology Information (NCBI) database (PRJNA658853 and PRJNA658721).

2.18. Statistical analysis

The results of at least 3 independent experiments are expressed as the mean ± SD. Differences between two groups and multiple groups were compared by two-tailed Student's *t*-test and one-way analysis of variance (ANOVA), respectively. $P < 0.05$ was considered statistically significant.

3. Results

3.1. Fabrication and characterization of DBM-MSN/152RM scaffolds

The DBM scaffolds were first constructed with negatively charged MSNs on their surface, and then positively charged 152RM was loaded. In this process, the presence of a negative charge on MSNs and a positive charge on 152RM allowed 152RM to be easily loaded on the surface of the DBM scaffolds (Fig. 1A). A total of four scaffolds (pure DBM scaffolds, intermediate DBM-MSN scaffolds, DBM/152RM scaffolds and DBM-MSN/152RM scaffolds) were fabricated for further analysis. Cross-sectional scanning electron microscopy (SEM) images revealed the microstructural features of the scaffolds (Fig. 1B). Transmission electron microscopy (TEM) showed that the MSN/152RM nanoparticles were spherical, with a size of approximately 60 nm (Figure S1A and B). The size of the pores in scaffolds is very important for the exchange of nutrients, oxygen, and metabolites and for neovascularization, which directly affects the growth of tissues [7]. In this study, the DBM scaffolds, DBM-MSN scaffolds, DBM/152RM scaffolds and DBM-MSN/152RM scaffolds had similar pores, with diameters of 419 ± 92 μm, 428 ± 86 μm, 426 ± 89 μm and 434 ± 84 μm, respectively (Fig. 1C). This is consistent with previous studies, which suggested that scaffolds with pore diameters between 100 μm and 1200 μm are ideal for bone regeneration [30]. SEM images also appeared to reveal that the surface microroughness of DBM-MSN/152RM scaffolds was increased, which indicated the presence of MSN and 152RM nanocrystals (Fig. 1B). To quantify the attachment of MSN to the scaffolds, the particles were analyzed by thermogravimetric analysis (TGA). Approximately 7% MSN (by weight) was incorporated into the DBM (Figure S1C). We further confirmed through oscillation experiments that MSN attachment to the DBM scaffold was relatively stable (Figure S1D). The surface charges of the MSNs and 152RM were −17.6 ± 1.9 and +14.9 ± 1.7, respectively, which supported the electrostatic attraction of cationic peptides (Figure S1E). The hydrodynamic diameter was not different between the MSN and MSN/152RM scaffolds (Figure S1F). This was confirmed by SEM-EDX, which showed that DBM-MSN/152RM scaffolds contain more silicon than other scaffolds (Fig. 1D). In this research, after 3 rounds of layer-by-layer assembly, 152RM reaches the maximum load, and the loading efficiency is 57.8 ± 2.4% (Figure S1G). The method to achieve the best coating efficiency was selected according to previous studies [31–33]. However, the amount of 152RM loaded into pure DBM was approximately 35.5 ± 2.2% (Figure S1G). The DBM-MSN/152RM scaffolds maintained a relatively slow and continuous release state (Fig. 1E). The steady release of 152RM can not only recruit MSCs and ECs to the bone defect site but also promote cell-matrix adhesion and extension on the scaffolds [12]. In addition, the BET surface area of DBM-MSN/152RM scaffolds increased from 2.5 m^2/g to 4.3 m^2/g (Table S2). The surface wettability of the scaffolds was evaluated by the contact angle measurement process, and the decreased contact angle value confirmed the increased hydrophilicity of the scaffolds. The contact angle of DBM, DBM-MSN, DBM/152RM and DBM-MSN/152RM scaffolds were 89.3° ± 2.1°, 89.1° ± 1.4°, 89.9° ± 1.8° and 88.2° ± 1.7°, respectively (Figure S1H). There is no significant difference among each group. The compressive strength of the DBM, DBM-MSN, DBM/152RM and DBM-MSN/152RM scaffolds were 331.5 ± 45.9 kPa,

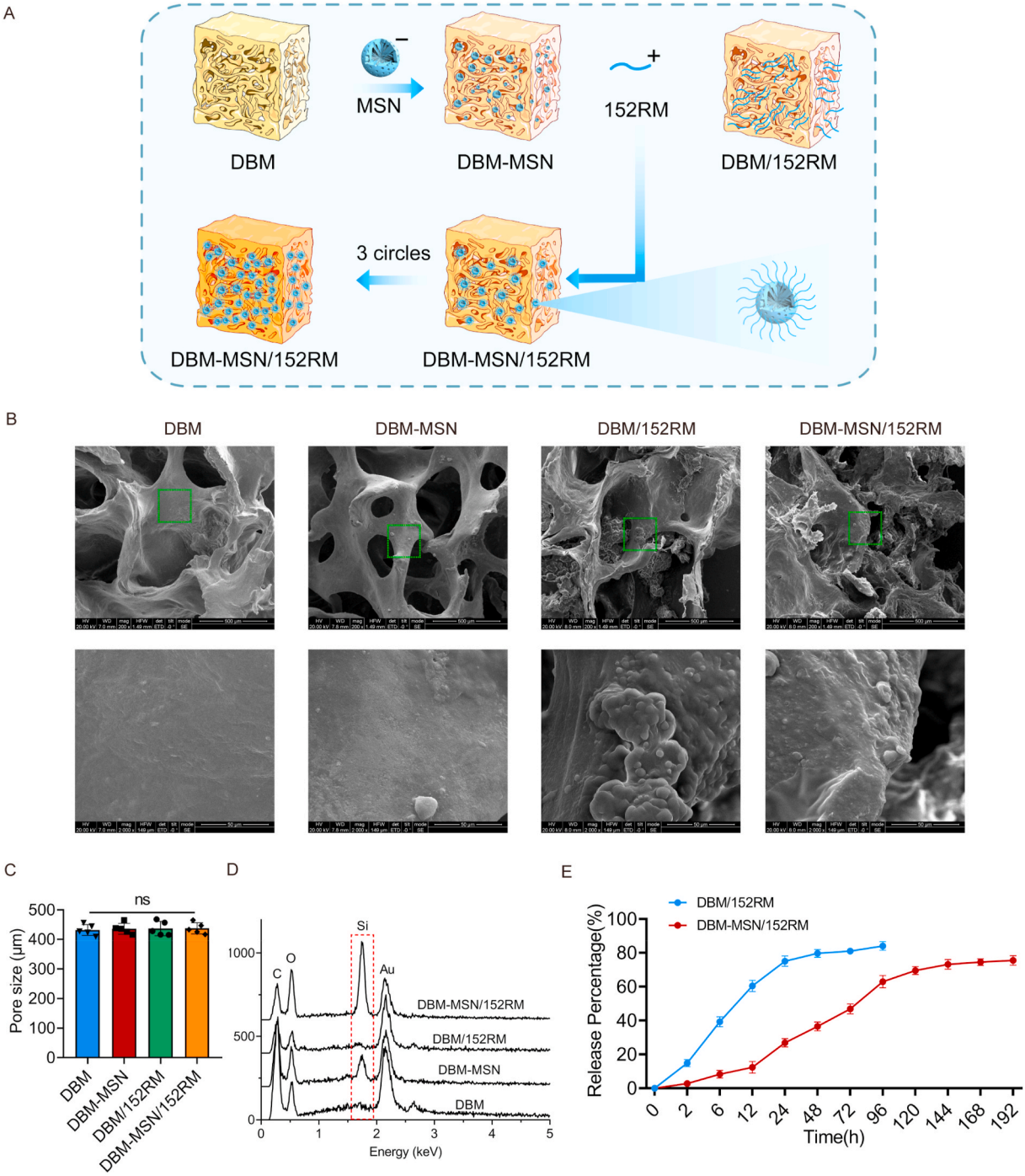

Fig. 1. Fabrication and characterization of DBM-MSN/152RM scaffolds. (A) Diagram showing the preparation process of DBM-152RM scaffolds, including layer-by-layer assembly with mesoporous silica nanoparticles (MSNs). (B) Cross-sectional scanning electron micrographs showing the scaffolds of the pure DBM scaffold (left), the DBM-MSN scaffold (middle), and the DBM-MSN/152RM scaffold (right). Scale bar, 100 μm. (C) Mean pore size of scaffolds. (D) Silicon element analysis of the four different scaffolds by using SEM-EDX. (E) Summarized data showing the 152RM release ratio over time for the DBM-MSN/152RM scaffolds *in vitro*. Data are shown as the mean ± SD. ns $p > 0.05$, ANOVA was employed. For all panels in this figure, the data are representative of three independent experiments.

323.3 ± 53.8 kPa, 319.9 ± 44.1 kPa, and 326.7 ± 51.2 kPa, respectively (Figure S1I). There is no statistical difference among each group. This indicates that the DBM-MSN/152RM scaffolds retain the mechanical strength of DBM, suggesting that they are sufficient for bone regeneration without weight-bearing application.

3.2. Determination of the biocompatibility of the scaffolds with MSCs and ECs

To elucidate the effects of the scaffolds on cell viability and proliferative activity, MSCs were cultured in the presence of scaffolds. After 24 h of culture, live/dead staining showed that more than 90% of the MSCs survived (Fig. 2A and B). Moreover, the CCK-8 assay revealed no significant difference in cell viability and proliferation activity after culture for 3 or 5 days (Fig. 2C). Cytoskeletal staining images indicated

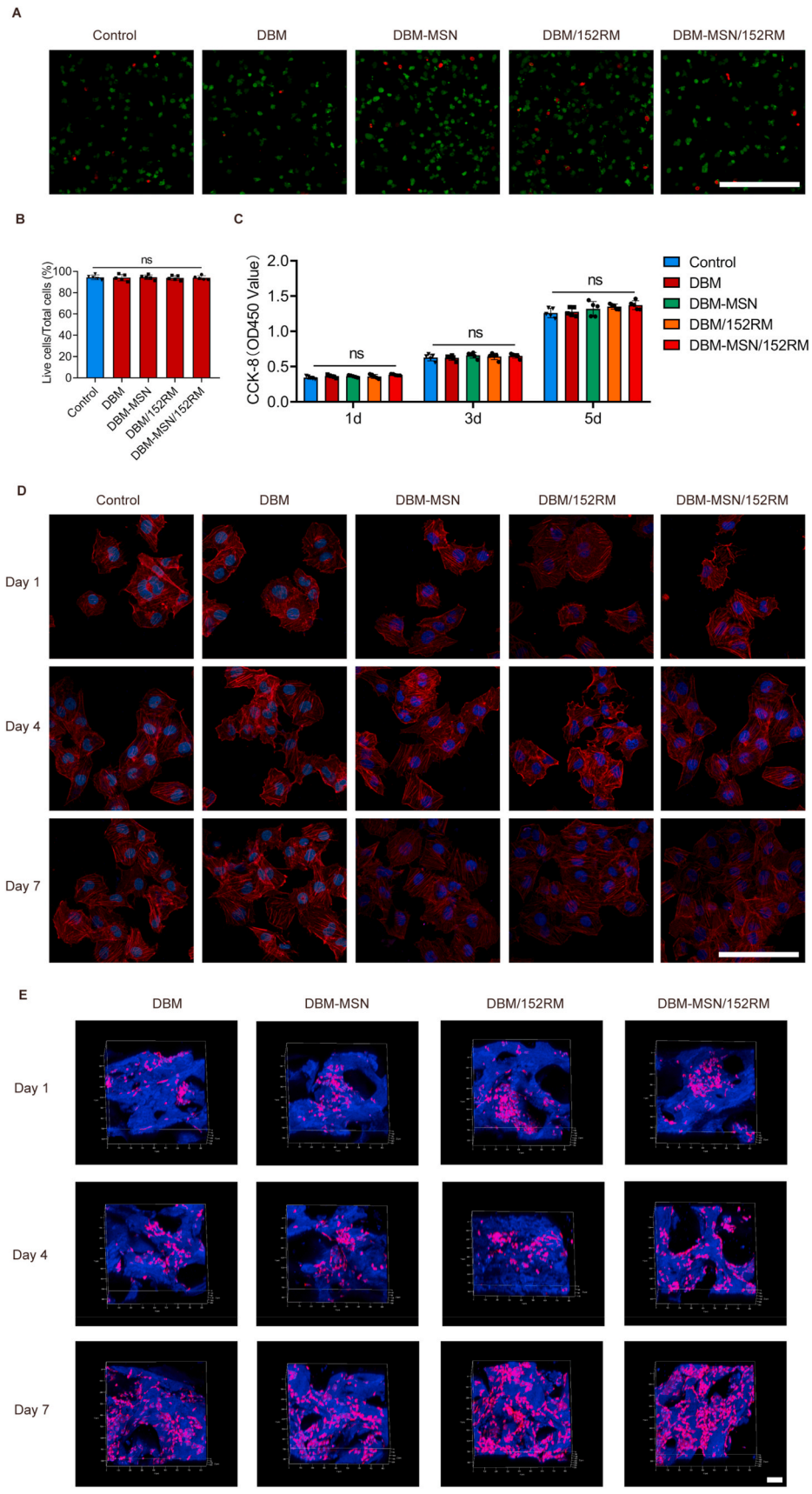

Fig. 2. Determination of the biocompatibility of the scaffolds with MSCs and ECs. (A, B) Live/dead assay showing cell viability after 24 h of culture on scaffolds. Live cells with esterase activity appeared green, whereas dead cells with compromised plasma membranes appeared red. Scale bar, 100 μm. (C) Cell Counting Kit-8 assay showing cell toxicity and proliferation after culturing the cells with the different scaffolds for 1, 3 and 5 days. Cells cultured without scaffolds were used as controls. Data are shown as the mean ± SD. ns $P > 0.05$. (D) High-resolution laser scanning confocal microscopy images of the cytoskeleton (red, phalloidin) and nuclei (blue, DAPI), showing MSCs cultured on identified scaffold struts for 1, 4 and 7 days. Scale bar, 100 μm. (E) Original confocal Z-stack images of MSCs (red, phalloidin; blue, DAPI) extending on the surface of identified scaffold struts (yellow, reflection ray) after culturing the cells for 1, 4 and 7 days. ns $p > 0.05$, ANOVA was employed. Scale bar, 100 μm.

that the MSCs on each scaffold presented good extension and proliferation status (Fig. 2D). The reconstructed confocal Z-stack images showed good adhesion and extension of cells along the surface of the scaffolds (Fig. 2E, Figure S2). These results showed that DBM-MSN/152RM scaffolds have good biocompatibility and no negative effect on the activity and morphology of growing cells.

3.3. 152RM induces the migration of MSCs partly through the FAK/STAT3 signaling pathway

To examine the role of 152RM in MSCs mobility, transwell chamber migration and scratch wound assays were performed. 152RM significantly stimulated more MSCs migration than the other treatments (Fig. 3A, Figure S3A-C). The RNA-seq results indicated that 152RM could enhance the expression of CXCR4 and integrin αvβ3 in MSCs (Fig. 3B). qRT-PCR confirmed that the transcription of CXCR4, integrin αv and integrin β3 increased 3.7-fold, 2.9-fold and 2.5-fold, respectively, in the presence of 152RM (Fig. 3C). Either the CXCR4 inhibitor AMD 3100 or the integrin αvβ3 inhibitor cyclo(-RGDfK) significantly inhibited MSCs migration (Fig. 3D, Figure S3C). Activation of FAK (focal adhesion kinase) is known to mediate cell migration [34]. We found that the phosphorylation of FAK was increased and the expression of E-cadherin was decreased (Fig. 3E and H; Figure S3D). Furthermore, GSEA of the RNA-seq results suggested that the JAK-STAT signaling pathway was activated (Fig. 3F and G). Western blotting confirmed that phosphorylation of STAT3 in MSCs increased after the addition of 152RM (Fig. 3H, Figure S3D). The level of p-STAT3 was reduced by inhibition of CXCR4, integrin αvβ3, or FAK (Fig. 3H, Figure S3D). Taken together, these results suggest that 152RM functions in part by inducing FAK/STAT3-dependent MSCs migration and inhibiting cadherin-mediated cell-cell adhesion (Fig. 4J).

3.4. 152RM induces osteogenic differentiation of MSCs by inhibiting endoplasmic reticulum stress, with downregulation of ATF3 expression

We then examined the effect of 152RM on the differentiation of MSCs. Under osteogenic induction culture conditions, the results of alkaline phosphatase staining and alizarin red staining demonstrated that 152RM could promote osteogenic differentiation of MSCs (Fig. 4A and B; Figure S4A). The molecular mechanism by which 152RM promotes MSCs differentiation was further investigated. RNA-seq indicated that ATF3 expression was downregulated in the 152RM group (Fig. 4C). qRT-PCR and western blotting confirmed that ATF3 expression was reduced by 65.5% after the addition of 152RM (Fig. 4D and E). ATF3 is an activated transcription factor that is associated with endoplasmic reticulum stress and can inhibit the activity of the Wnt/β-catenin signaling pathway [35]. Western blotting analysis indicated that the level of the endoplasmic reticulum stress marker CHOP was decreased in the 152RM group (Fig. 4E). Immunofluorescence showed that 152RM promoted the nuclear translocation of β-catenin, and overexpression of ATF3 induced by tunicamycin inhibited the nuclear translocation of β-catenin (Fig. 4F; Figure S4B). After IWR-1 inhibited the Wnt/β-catenin pathway, the expression levels of osterix, osteopontin (OPN), runt-related transcription factor 2 (Runx2) and osteocalcin (OCN) partly decreased (Fig. 4G–I; Figure S4C). These results suggested that 152RM activates the Wnt/β-catenin signaling pathway to promote osteogenic differentiation, partly by inhibiting endoplasmic reticulum stress, with downregulation of ATF3 expression (Fig. 4J).

3.5. 152RM induces ECs migration partly through the FAK/ERK signaling pathway

PTP1B plays an important role in regulating the extent of vascular tree formation via endothelial VEGFR2 signaling [36]. 152RM was also demonstrated to significantly promote ECs migration (Fig. 5A, Figure S5A-C). qRT-PCR indicated that 152RM promoted the expression of integrin αvβ3 and VEGFR2 in ECs (Fig. 5B). Integrin αvβ3 and VEGFR2 both play an important role in angiogenesis, and there is close crosstalk between them [37]. The expression levels of integrin αvβ3 and VEGFR2 were both increased after the addition of 152RM (Fig. 5C, E). The migration of ECs was significantly partly abolished by the integrin αvβ3 inhibitor cyclo(-RGDfK) or the VEGFR2 inhibitor Ki8751 (Fig. 5D). Activation of FAK is known to mediate cell migration and angiogenesis [38]. Western blotting analysis demonstrated that 152RM increased the phosphorylation level of FAK, thereby activating the downstream ERK signaling pathway (Fig. 5E; Figure S5D-G). Altogether, our results show that 152RM induces FAK/ERK-dependent ECs migration by enhancing the crosstalk between integrin αvβ3 and VEGFR2 signaling (Fig. 5F).

3.6. 152RM promotes angiogenesis via the endothelial Notch signaling pathway in vitro

To determine whether 152RM promotes angiogenesis *in vitro*, we performed a tube formation assay and found that 152RM significantly enhanced ECs tube formation (Fig. 6A). Interestingly, the presence of MSCs further enhanced 152RM-mediated ECs tube formation, suggesting that MSCs and 152RM have a synergistic effect. Furthermore, GSEA of the RNA-seq results suggested that the endothelial Notch signaling pathway was activated (Fig. 6B and C). qRT-PCR demonstrated that 152RM increased the expression levels of DLL4, DLL3, Jag1, Notch1 and Notch2 in ECs (Fig. 6D). The expression of target genes (Hes1, Hes7, and Hey1) and noggin in the Notch pathway was also increased compared with that in the control (Fig. 6D). Immunofluorescence also revealed that 152RM could upregulate the expression of DLL4 and Notch1 in ECs (Fig. 6E and F). The angiogenic capacity of 152RM was apparently abolished by the Notch pathway antagonist IMR-1A (Fig. 6G). Moreover, 152RM stimulated ECs to secrete noggin, which coupled angiogenesis and bone formation (Fig. 6H). These results indicate that 152RM induces angiogenesis via a Notch-dependent mechanism. In addition, 152RM-stimulated MSCs secreted approximately 3.9-fold more VEGF than the control MSCs (Supplementary Figure 6A, B). However, we found no change in VEGF derived from endothelial cells treated with 152RM (Figure S6 C, D). Overall, 152RM could induce the formation of vessels partly by activating the endothelial Notch signaling pathway (Fig. 6I).

3.7. DBM-MSN/152RM scaffolds coordinate the recruitment of MSCs and ECs in vivo

To verify the cell recruitment capacity of each scaffold *in vivo*, we collected specimens one week after implantation. HE staining revealed that DBM-MSN/152RM scaffolds recruited more nucleated cells than other scaffolds (Fig. 7A). Moreover, immunofluorescence indicated that the number of cells copositive for CXCR4, integrin αvβ3 and CD271 in DBM-MSN/152RM scaffolds was greater than those in other scaffolds (Fig. 7B). Analysis of CD90 and CD105 double-positive cells also confirmed that DBM-MSN/152RM scaffolds had the strongest ability to recruit MSCs (Fig. 7C). Similarly, the largest number of integrin αvβ3 and emcn double-positive cells was found in DBM-MSN/152RM scaffolds (Fig. 7D). CD31-positive cells also confirmed that DBM-MSN/152RM scaffolds had the strongest ability to recruit ECs among these scaffolds (Fig. 7E). These results indicate that DBM-MSN/152RM scaffolds can coordinate the simultaneous recruitment of MSCs and ECs *in vivo*.

3.8. DBM-MSN/152RM scaffolds induce angiogenesis in vivo

A blood supply is essential for bone formation. Histological images of the specimens were obtained two weeks after implantation. No obvious inflammatory reaction or necrosis was observed in any group, and newly formed bone, fibrous tissue and scaffolds were observed. As predicted, the DBM-MSN/152RM scaffolds presented a large number of new blood vessels (Fig. 8A). Specifically, microfil-perfused angiography revealed

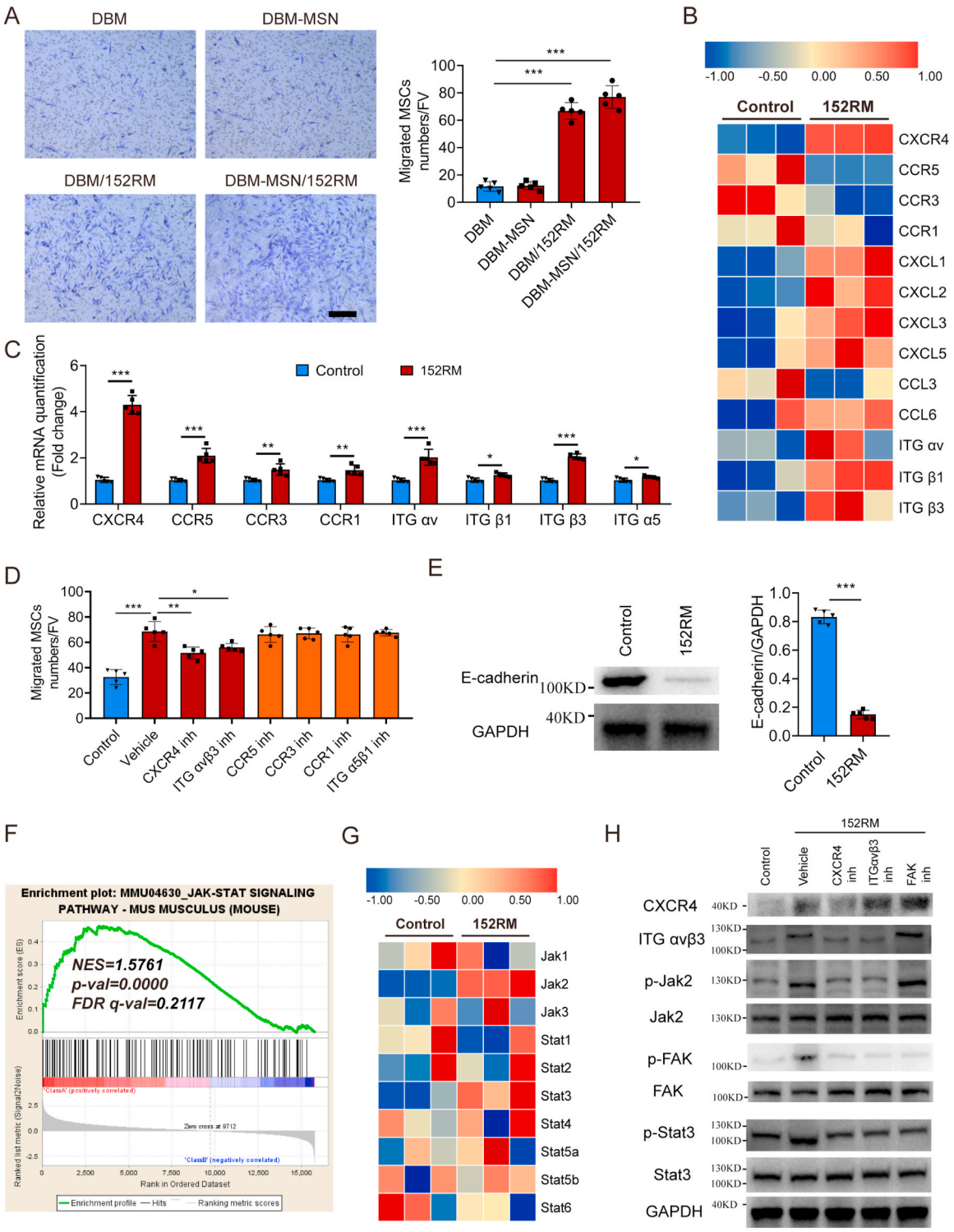

Fig. 3. 152RM induces the migration of MSCs partly through the FAK/STAT3 signaling pathway. (A) Transwell assays for the migration of MSCs using 152RM (n = 5 each). Representative crystal violet staining images are shown in the left panel. Quantification of cell migration is shown in the right panel. Scale bar, 100 μm. (B) RNA-seq analysis showed the alteration of cell migration-specific gene expression in MSCs cultured with 152RM (n = 3 each). (C) Relative mRNA expression levels of cell migration-specific genes in MSCs cultured with 152RM (n = 5 each). (D) Quantification of the transwell assay and cell wound scratch assay after culture with 152RM, a CXCR4 inhibitor (AMD3100) and an Integrin αvβ3 inhibitor (Cyclo(-RGDfK)) (n = 5 each). (E) Western blot analysis of the expression of E-cadherin in MSCs after the addition of 152RM (n = 5 per group). (F) Gene set enrichment analysis (GSEA) plots showing upregulation of the JAK/STAT signaling pathway in MSCs cultured with 152RM (n = 3 each). (G) RNA-seq analysis showed alterations in JAK/STAT signaling pathway-related gene expression in MSCs cultured with 152RM (n = 3 each). (H) Western blot analysis of the expression of CXCR4, integrin αvβ3, p-Jak2, Jak2, p-FAK, FAK, p-STAT3 and STAT3 in MSCs (pretreated with a CXCR4 inhibitor (AMD3100) and an integrin αvβ3 inhibitor (cyclo(-RGDfK))) after the addition of 152RM (n = 5 per group). Data are shown as the mean ± SD. *P < 0.05, **P < 0.01, ***P < 0.001; ANOVA and Student's *t*-test were employed. For all panels in this figure, data are representative of three independent experiments.

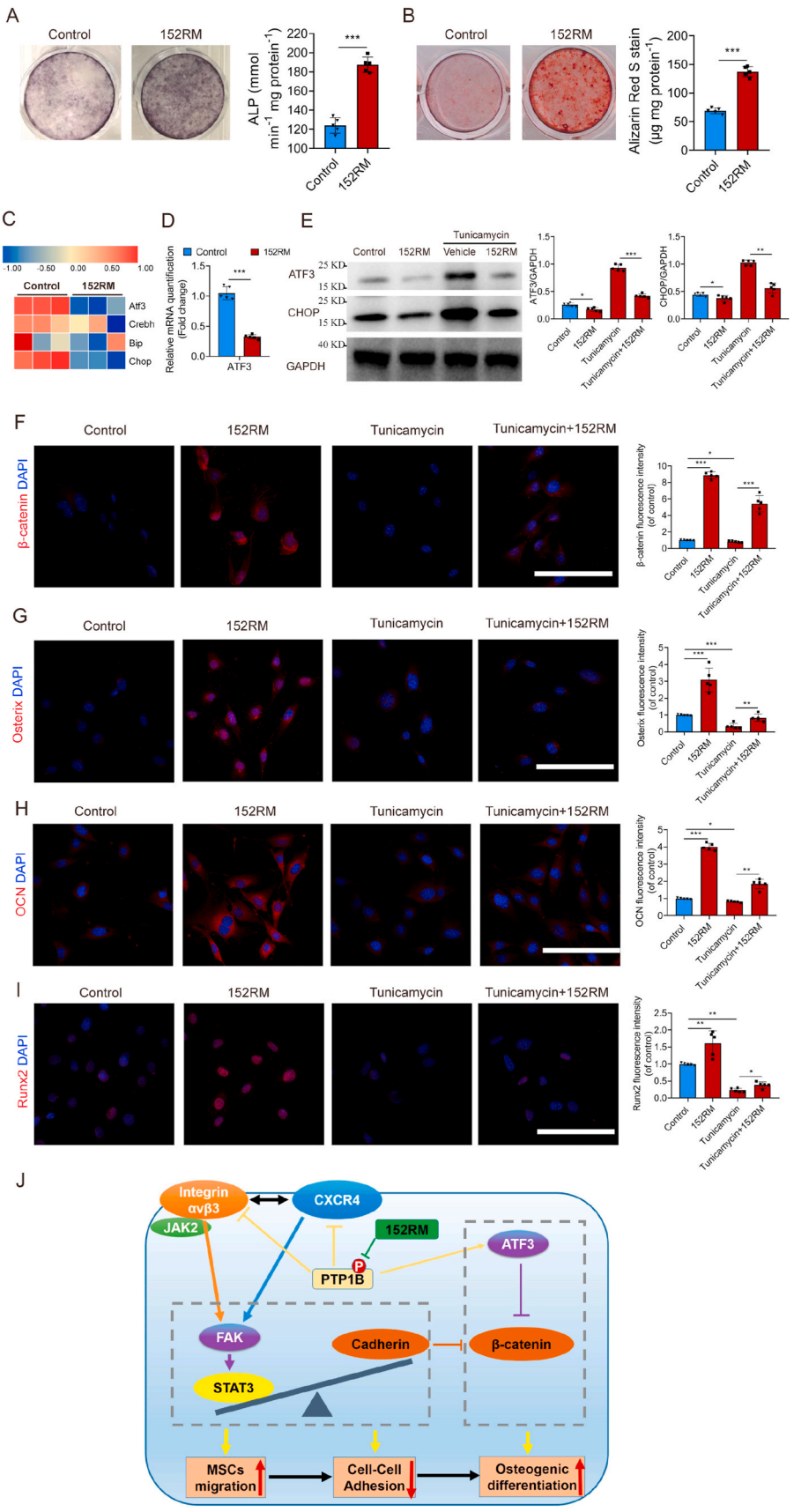

Fig. 4. 152RM induces osteogenic differentiation of MSCs by inhibiting endoplasmic reticulum stress, with downregulation of ATF3 expression. (A) MSCs were induced to differentiate into mature OBs in osteogenic differentiation medium without or with 152RM after 14 days. Representative alkaline phosphatase staining images (left) and quantification of the activity of alkaline phosphatase were performed (right) (n = 5 per group). (B) MSCs were induced to differentiate into mature OBs in osteogenic differentiation medium without or with 152RM after 21 days. Representative Alizarin red staining images (left) and quantification of matrix mineralization (right) (n = 5 per group). (C) RNA-seq analysis showed the alteration of endoplasmic reticulum stress-related gene expression in MSCs cultured with 152RM (n = 3 each). (D) Relative mRNA expression levels of ATF3 in MSCs cultured with 152RM (n = 5 each). (E) Western blot analysis of the expression of ATF3 and CHOP in MSCs (pretreated with 5 ng/mL tunicamycin) after the addition of 152RM (n = 5 per group). (F) Representative immunostaining images of β-catenin (red) MSCs or MSCs pretreated with 5 ng/mL tunicamycin in osteogenic differentiation medium with 152RM after 14 days (n = 5 per group). Scale bar, 100 μm. (G) Representative immunostaining images of osterix (red) MSCs or MSCs pretreated with 5 ng/mL tunicamycin in osteogenic differentiation medium with 152RM after 14 days (n = 5 per group). Scale bar, 100 μm. (H) Representative immunostaining images of osteocalcin (red) MSCs or MSCs pretreated with 5 ng/mL tunicamycin in osteogenic differentiation medium with 152RM after 14 days (n = 5 per group). Scale bar, 100 μm. (I) Representative immunostaining images of Runx2 (red) MSCs or MSCs pretreated with 5 ng/mL tunicamycin in osteogenic differentiation medium with 152RM after 14 days (n = 5 per group). Scale bar, 100 μm. (J) Schematic illustration of the role of 152RM in promoting MSC migration and osteogenic differentiation. Data are shown as the mean ± SD. *P < 0.05, **P < 0.01, ***P < 0.001; ANOVA and Student's *t*-test were employed. For all panels in this figure, data are representative of three independent experiments.

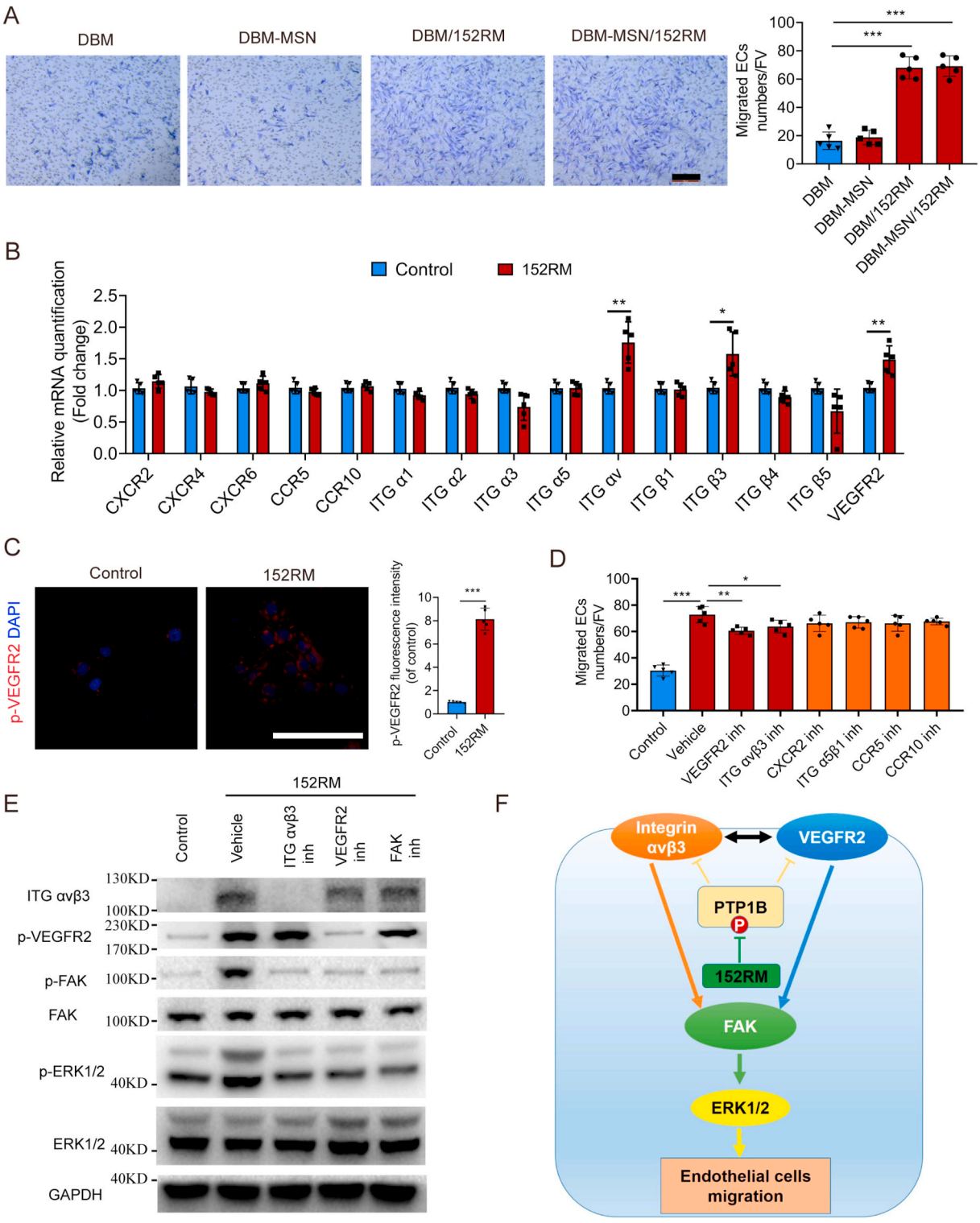

Fig. 5. 152RM induces ECs migration partly through the FAK/ERK signaling pathway. (A) Transwell assay for the migration of ECs using 152RM (n = 5 each). Scale bar, 100 μm. Quantification of cell migration was performed (right). (B) Relative mRNA expression levels of cell migration-specific genes in ECs cultured with 152RM (n = 5 each). (C) Representative immunostaining images of p-VEGFR2 (red) ECs with or without 152RM (n = 5 per group). Scale bar, 100 μm. (D) Quantification of transwell assays after culture with 152RM, a VEGFR2 inhibitor (Ki8751) and an integrin αvβ3 inhibitor cyclo(-RGDfK) (n = 5 each). (E) Western blot analysis of the expression of integrin αvβ3, p-VEGFR2, p-FAK, FAK, p-ERK1/2 and ERK1/2 in ECs (pretreated with a VEGFR2 inhibitor (Ki8751) and an integrin αvβ3 inhibitor (cyclo(-RGDfK))) after the addition of 152RM (n = 5 per group). (F) Schematic illustration of the role of 152RM in promoting ECs migration. Data are shown as the mean ± SD. *P < 0.05, **P < 0.01, ***P < 0.001; ANOVA and Student's *t*-test were employed. For all panels in this figure, data are representative of three independent experiments.

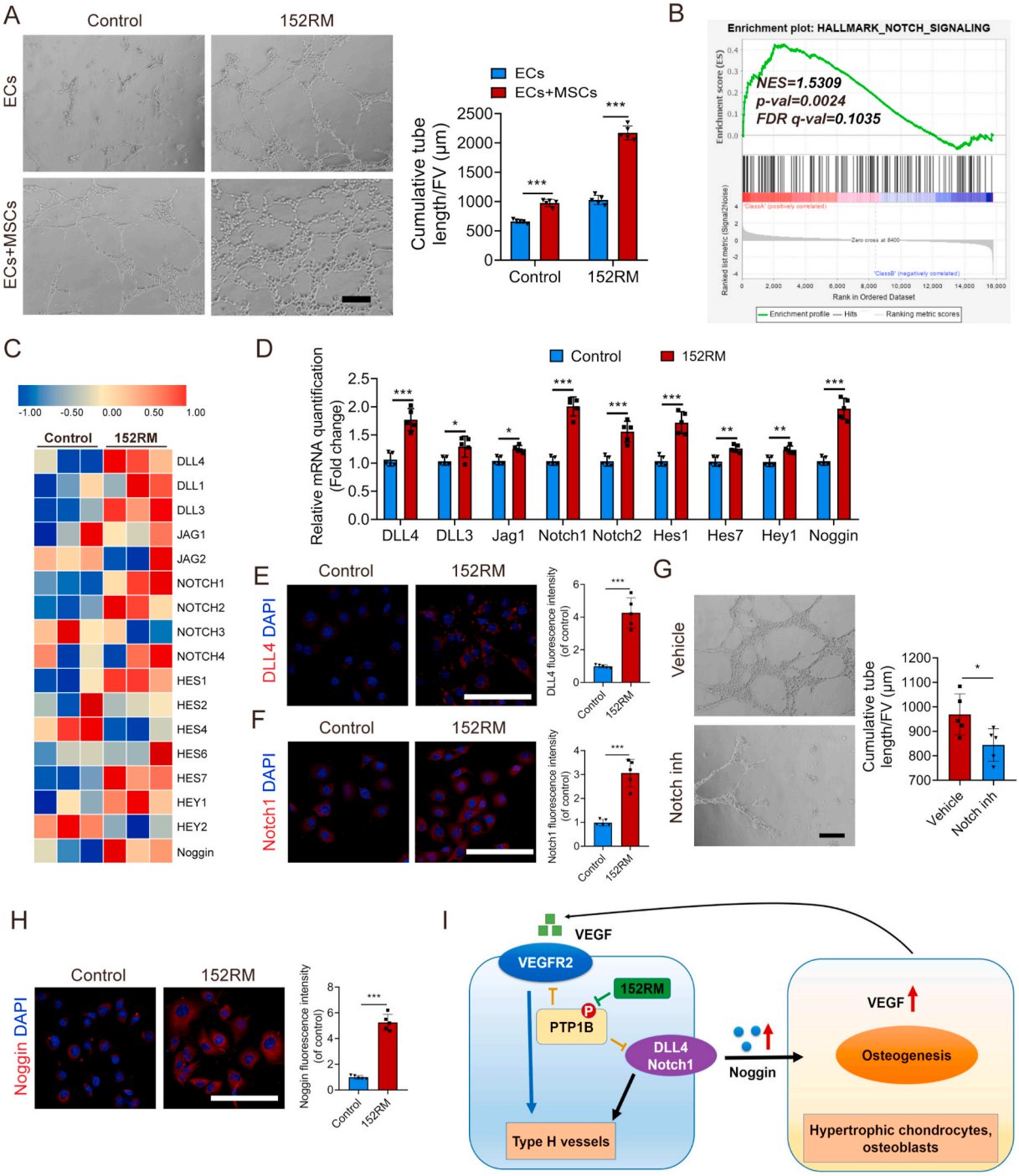

Fig. 6. 152RM promotes angiogenesis via the Notch signaling pathway. (A) Representative images of tube formation by ECs (with or without coculture with MSCs) after the addition of 152RM. Scale bar, 100 μm. The quantitative analysis of cumulative tube length is shown in the right panel (n = 5 per group). (B) Gene set enrichment analysis (GSEA) plots showing upregulation of the Notch signaling pathway in ECs cultured with 152RM (n = 3 per group). (C) RNA-seq analysis showed alterations in Notch signaling pathway-related gene expression in ECs cultured with 152RM (n = 3 per group). (D) Relative mRNA expression levels of Notch signaling pathway-related genes in ECs cultured with 152RM (n = 5 each). (E) Representative immunostaining images of DLL4 (red) ECs with 152RM (n = 5 per group). Scale bar, 100 μm. (F) Representative immunostaining images of Notch1 (red) ECs with 152RM (n = 5 per group). Scale bar, 100 μm. (G) Representative images of tube formation by ECs treated with 152RM (with or without Notch inhibitor). n = 5 per group. Scale bar, 100 μm. (H) Representative immunostaining images of Noggin (red) ECs with 152RM (n = 5 per group). Scale bar, 100 μm. (I) Schematic illustration of the role of 152RM in inducing the formation of type H vessels and coupling osteogenesis and angiogenesis. Data are shown as the mean ± SD. *P < 0.05, **P < 0.01, ***P < 0.001; Student's *t*-test was employed. For all panels in this figure, data are representative of three independent experiments.

that there was a rich vascular network in the center of the DBM-MSN/152RM scaffolds, and the vessel volume and vessel surface area were greater than those of the other scaffolds 8 weeks after implantation (Fig. 8B). Moreover, the DBM-MSN/152RM scaffolds displayed a significant increase in the number of $CD31^{hi}Emcn^{hi}$ ECs (type H vessels) in the bone defects (Fig. 8C). At the same time, the proliferation ability of $CD31^{hi}Emcn^{hi}$ vessels was also enhanced on the DBM-MSN-152RM scaffolds (Fig. 8D). In line with the key role of $CD31^{hi}Emcn^{hi}$ ECs in

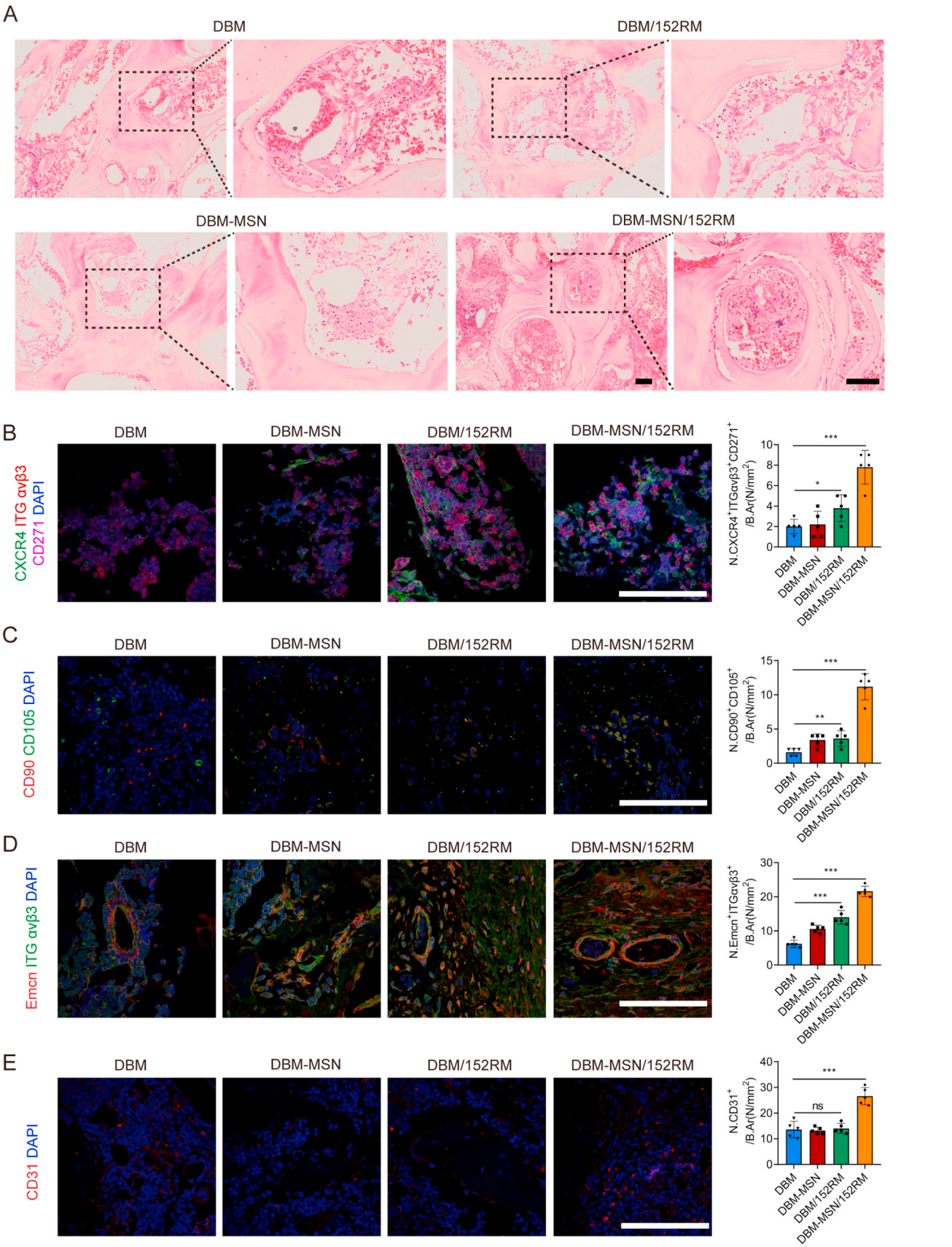

(caption on next page)

Fig. 7. DBM-MSN/152RM scaffolds coordinate the recruitment of MSCs and ECs *in vivo*. (A) HE staining images demonstrating the recruitment of MSCs and ECs 1 week after DBM, DBM-MSN, DBM/152RM and DBM-MSN/152RM scaffold implantation (n = 5 rats per group). Scale bar, 100 μm. (B) Co-immunofluorescence staining of CXCR4, integrin αvβ3 and CD271 in MSCs from 1 week after DBM, DBM-MSN, DBM/152RM and DBM-MSN/152RM scaffold implantation (n = 5 rats per group). Scale bar, 100 μm. (C) Immunofluorescence staining of $CD90^+CD105^+$ MSCs from 1 week after DBM, DBM-MSN, DBM/152RM and DBM-MSN/152RM scaffold implantation (n = 5 rats per group). Scale bar, 100 μm. (D) Co-immunofluorescence staining of emcn and integrin αvβ3 in type H vessels from 4 weeks after DBM, DBM-MSN, DBM/152RM and DBM-MSN/152RM scaffold implantation (n = 5 rats per group). Scale bar, 100 μm. (E) Immunofluorescence staining of $CD31^+$ in EPCs from 4 weeks after DBM, DBM-MSN, DBM/152RM and DBM-MSN/152RM scaffold implantation (n = 5 rats per group). Scale bar, 100 μm. Data are shown as the mean ± SD. ns $P > 0.05$, *$P < 0.05$, **$P < 0.01$, ***$P < 0.001$; ANOVA was employed. For all panels in this figure, data are representative of three independent experiments.

bone blood vessel growth and osteogenesis, the abundance of this cell population increased upon activation of endothelial Notch. Immunostaining confirmed high expression of DLL4 and emcn in new vessels of DBM-MSN/152RM scaffolds (Fig. 8E). Intriguingly, these cells were mainly distributed in the long fusiform endothelial cells around the new bone. These results suggested that local release of 152RM from DBM-MSN/152RM scaffolds activated the Notch signaling pathway and promoted a substantial expansion of type H vessels.

3.9. DBM-MSN/152RM scaffolds promote bone regeneration in vivo

X-ray and micro-CT were used to scan the bone defect area at 4 weeks and 8 weeks after implantation of the scaffolds. The DBM-MSN/152RM scaffolds showed more new bone formation than the other scaffolds. Moreover, the new bone integrated thoroughly with not only the periphery but also the center of the DBM-MSN/152RM scaffolds (Fig. 9A; Figure S7A). Quantitative micro-CT analysis showed that bone mineral density (BMD), bone tissue volume/total tissue volume (BV/TV), and number of trabecular bone (Tb.N) were significantly higher in the DBM-MSN/152RM scaffolds than in the other scaffolds, while the trabecular space (Tb.Sp) showed the opposite pattern (Fig. 9B). Further histomorphological investigations showed that DBM-MSN/152RM scaffolds had a stronger capacity to generate new bone (Fig. 9C and D; Figure S7B, C). Immunofluorescence staining images showed that DBM-MSN/152RM scaffolds had more bone progenitor cells and osteoblasts than other scaffolds (Fig. 10A and B). Importantly, histological analysis of undecalcified bone showed that both the MAR and BFR/BS were increased in the DBM-MSN/152RM scaffold group (Fig. 10C). In addition, von kossa staining revealed the highest level of calcification in DBM-MSN/152RM scaffolds at 8 weeks (Fig. 10D). Taken together, these results show that DBM-MSN/152RM scaffolds had a stronger ability to regenerate bone than other scaffolds.

4. Discussion

Bone defect repair remains a challenge in modern medicine, with substantial social and economic burdens [1]. Although great progress has been made in research on the use of bioactive scaffolds for bone regeneration in recent years [39], MSCs and ECs are still considered to be critical for initiating bone healing [40]. In fact, evidence for the efficacy of MSCs in promoting bone regeneration comes not only from the ability of MSCs to reverse skeletal metabolic diseases but also from the successful application of MSCs in bone tissue engineering and cell therapy [41,42]. However, although MSC-mediated bone repair has shown great promise, it is still difficult to recruit MSCs to the bone defect site. Therefore, there is an urgent need to optimize the methods used to recruit MSCs from their niches to bone defect sites. In our study, we showed that 152RM released from DBM-MSN/152RM scaffolds can promote bone regeneration by coupling osteogenesis with angiogenesis (Fig. 11).

PTP1B is a ubiquitously expressed nonreceptor phosphatase that is targeted to several intracellular sites, including the endoplasmic reticulum and focal adhesions. PTP1B plays a key role in mediating cadherin-dependent intercellular adhesion and integrin-dependent cell migration [43]. Phosphorylation of PTP1B Y152 results in dephosphorylation of β-catenin, which stabilizes cadherin and enhances cell adhesion to the extracellular matrix [11]. Therefore, we hypothesized that inhibition of PTP1B Y152 phosphorylation would not only attenuate cadherin-mediated cell-matrix adhesion but also promote integrin-mediated cell migration. To further verify this hypothesis, we previously synthesized a novel peptide (152RM) that contained 26 amino acids and could efficiently enter cells [44].

To achieve stable and slow release of 152RM *in vivo*, mesoporous silica nanoparticles (MSNs) were used to load 152RM on the surface of DBM scaffolds. MSNs, a new type of nanomaterial, have the advantages of a high specific surface area, a large pore volume, a uniform pore size distribution, and good biocompatibility and can be used as a good carrier for many drugs [15]. We modified the surface of DBM scaffolds with 152RM peptide loaded on negative MSNs by electrostatic adsorption. DBM-MSN/152RM scaffolds have good biocompatibility and achieve the slow release of polypeptides. Our results show that MSNs can increase the BET surface area of DBM by approximately 60%, which can greatly increase the loading capacity of 152RM. Furthermore, DBM-MSN/152RM scaffolds were demonstrated to have the capacity to recruit more MSCs and ECs to bone defects than other scaffolds *in vivo*.

Then, we further investigated the possible mechanism by which 152RM can initiate cell recruitment. Our study showed that 152RM can increase the expression levels of CXCR4 and integrin αvβ3 on MSCs and enhance the crosstalk between them. Then, the downstream FAK/STAT3 signaling pathway was further activated to induce MSC migration. Consistent with previous studies, the 152RM peptide rapidly activates the phosphorylation of FAK, leading to dissociation of the cadherin complex and initiation of MSC departure from stem cell niches [44]. CXCl12/CXCR4 can directly activate the integrin αvβ3 signaling pathway and then promote cell migration [45]. Activation of integrin αvβ3 is associated with invasion and metastasis of multiple tumors [46]. However, the recruitment of MSCs in the bone defect microenvironment has not been reported. The mobilization ability of MSCs has been reported to be regulated by integrin αvβ3 [47]. Activation of the integrin signaling pathway is associated with subsequent osteogenic differentiation of MSCs [48]. Additionally, integrin αvβ3 mediates phagocytosis of apoptotic bodies to inhibit Axin1, activate the Wnt/β-catenin pathway, and promote osteogenic differentiation of MSCs [49]. A previous study by our group found that hCTLA4 gene-modified MSCs enhanced the migration ability of allogeneic MSCs through the integrin αvβ3/FAK pathway [50]. *In vivo* experiments also confirmed that DBM-MSN/152RM scaffolds recruit a large number of MSCs to bone defects. Altogether, these findings show that 152RM relies on the FAK/STAT3 signaling pathway to promote MSC migration by enhancing the crosstalk between CXCR4 and integrin αvβ3.

Bone defects can cause traumatic stress and excessive secretion of inflammatory factors such as TNF-α and IL-1β in the bone marrow [51]. Then, the level of endoplasmic reticulum (ER) stress represented by activation transcription factor 3 (ATF3) is increased, which mediates the inhibitory effect of TNF-α on osteogenic differentiation [52]. ATF3 is a member of the ATF/cAMP response element binding protein family, which is involved in regulating cell proliferation and differentiation. The expression of ATF3 is induced by ER stress in osteoblasts, which can inhibit ALP expression [53]. In our study, 152RM decreased ATF3 levels and induced MSCs to undergo osteogenic differentiation. Moreover, 152RM induces β-catenin to enter the nucleus to activate wnt signaling. It has been reported that the overexpression of Runx2 in osteoblasts

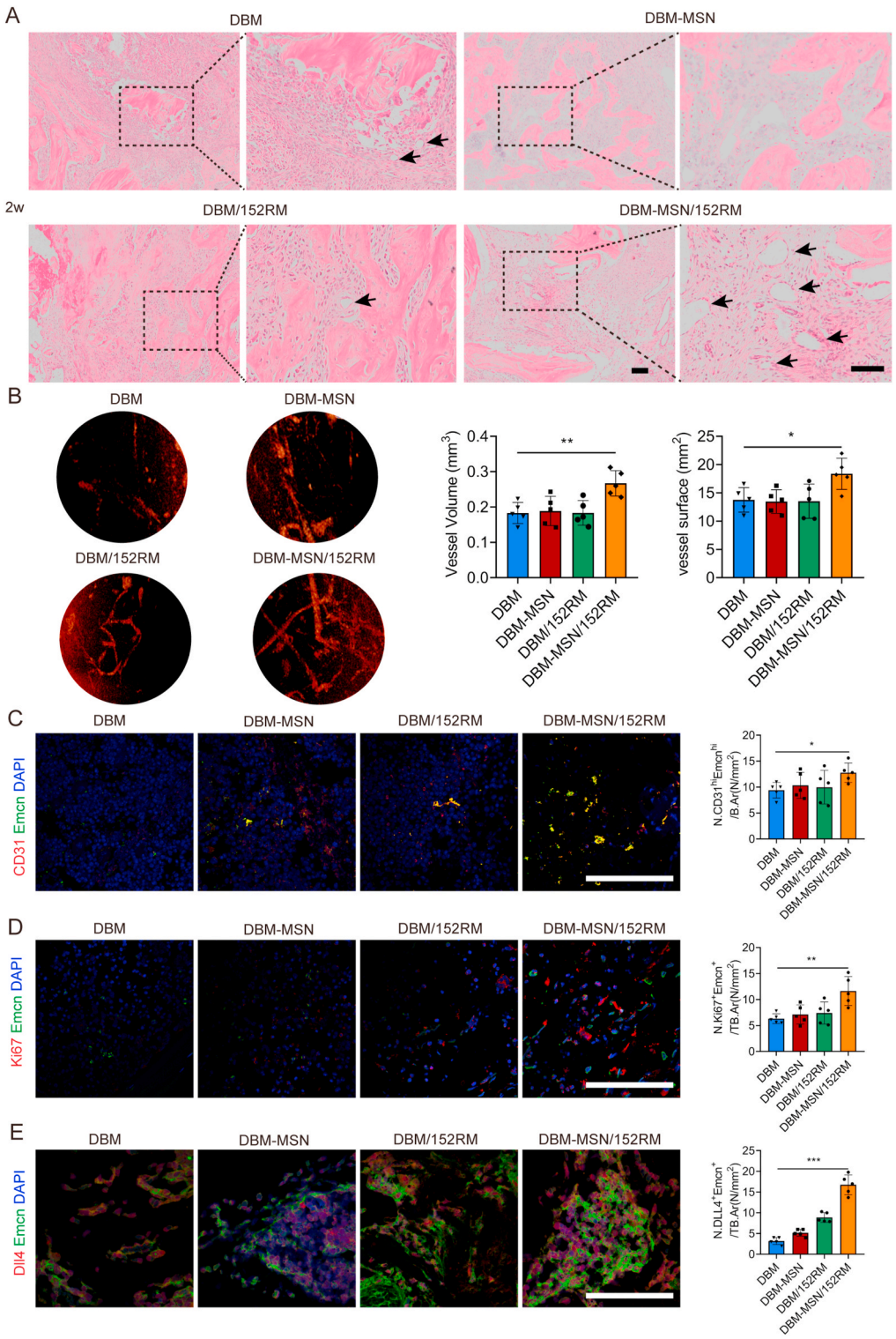

Fig. 8. DBM-MSN/152RM scaffolds induce angiogenesis *in vivo*. (A) HE staining images demonstrating angiogenesis 2 weeks after DBM, DBM-MSN, DBM/152RM and DBM-MSN/152RM scaffold implantation (n = 5 rats per group). Scale bar, 100 μm. (B) Representative angiographic images are shown in the left panel. Angiographic analysis of the volume and surface area of bone vessels 8 weeks after DBM, DBM-MSN, DBM/152RM and DBM-MSN/152RM scaffold implantation (n = 5 rats per group). Scale bar, 1 mm. (C) Representative immunostaining images of CD31 (red) and Emcn (green) in the BM (left) 8 weeks after DBM, DBM-MSN, DBM/152RM and DBM-MSN/152RM scaffold implantation. The quantification of $CD31^{hi}$ $Emcn^{hi}$ (yellow) cells is shown in the right panel (n = 5 rats per group). Scale bar, 100 μm. (D) Representative immunostaining images of Emcn (green) and Ki67 (red) in the BM (left) 8 weeks after DBM, DBM-MSN, DBM/152RM and DBM-MSN/152RM scaffold implantation. The quantification of Ki67 and Emcn cells is shown in the right panel (n = 5 rats per group). Scale bar, 100 μm. (E) Representative immunostaining images of Emcn (green) and DLL4 (red) in type H vessels from 4 weeks after DBM, DBM-MSN, DBM/152RM and DBM-MSN/152RM scaffold implantation (n = 5 rats per group). Scale bar, 100 μm. Data are shown as the mean ± SD. *P < 0.05, **P < 0.01, ***P < 0.001; ANOVA was employed. For all panels in this figure, data are representative of three independent experiments.

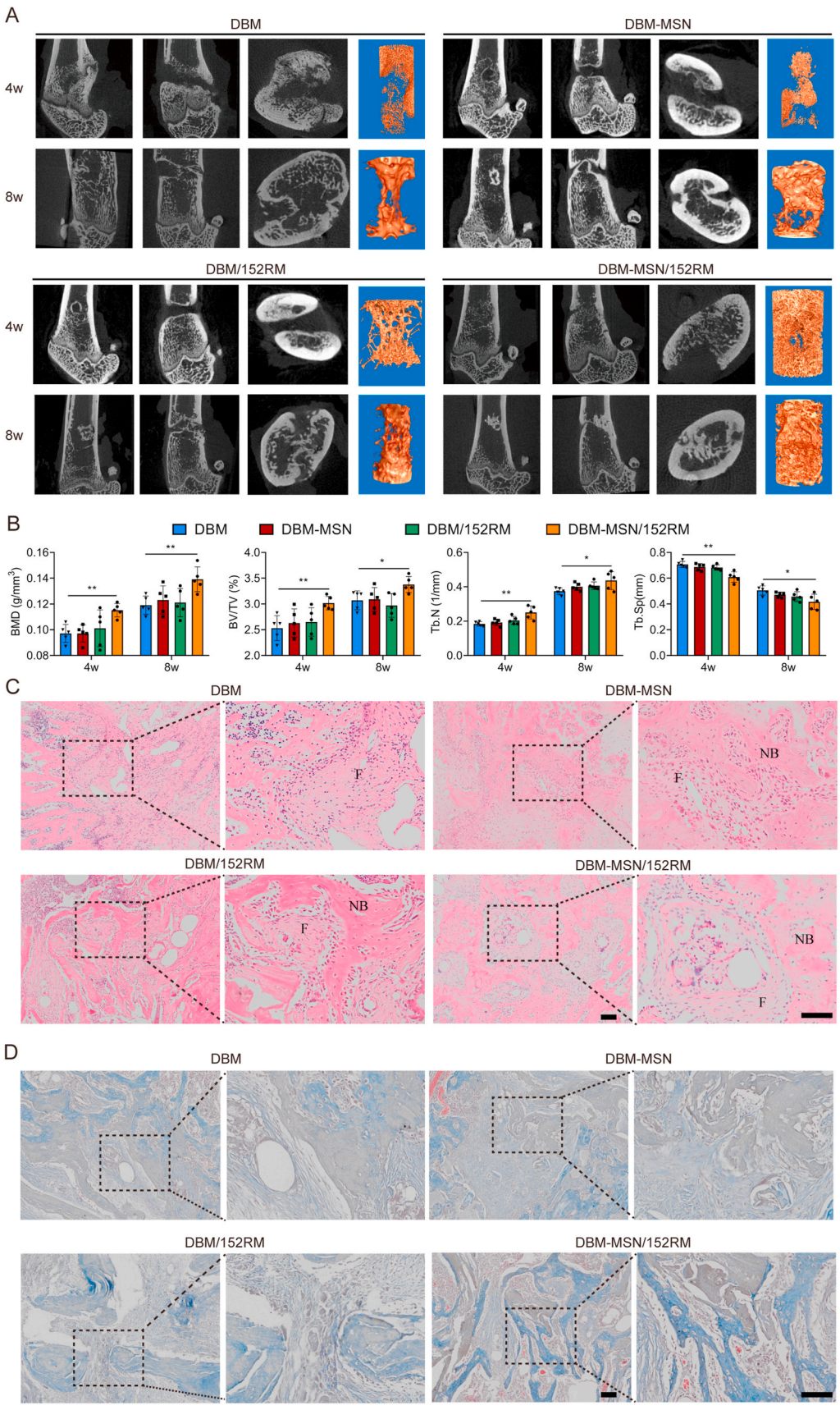

Fig. 9. DBM-MSN/152RM scaffolds promote bone regeneration *in vivo*. (A) Representative micro-CT images of longitudinal sections of femurs (sagittal plane and coronal plane) and cross-sectional view of the femurs 4 and 8 weeks after DBM, DBM-MSN, DBM/152RM and DBM-MSN/152RM scaffold implantation. (n = 5 rats per group). (B) Quantitative micro-CT analysis of the bone mineral density (BMD) and trabecular bone fraction (BV/TV, Tb.N and Tb.Sp) 4 and 8 weeks after DBM, DBM-MSN, DBM/152RM and DBM-MSN/152RM scaffold implantation. (n = 5 rats per group). (C) HE staining images demonstrating bone regeneration 4 weeks after DBM, DBM-MSN, DBM/152RM and DBM-MSN/152RM scaffold implantation (n = 5 rats per group). Scale bar, 100 μm. (D) Masson staining images demonstrating bone regeneration 4 weeks after DBM, DBM-MSN, DBM/152RM and DBM-MSN/152RM scaffold implantation (n = 5 rats per group). Scale bar, 100 μm. Scale bar, 50 μm. Data are shown as the mean ± SD. *P < 0.05, **P < 0.01, ***P < 0.001; ANOVA was employed. For all panels in this figure, data are representative of three independent experiments.

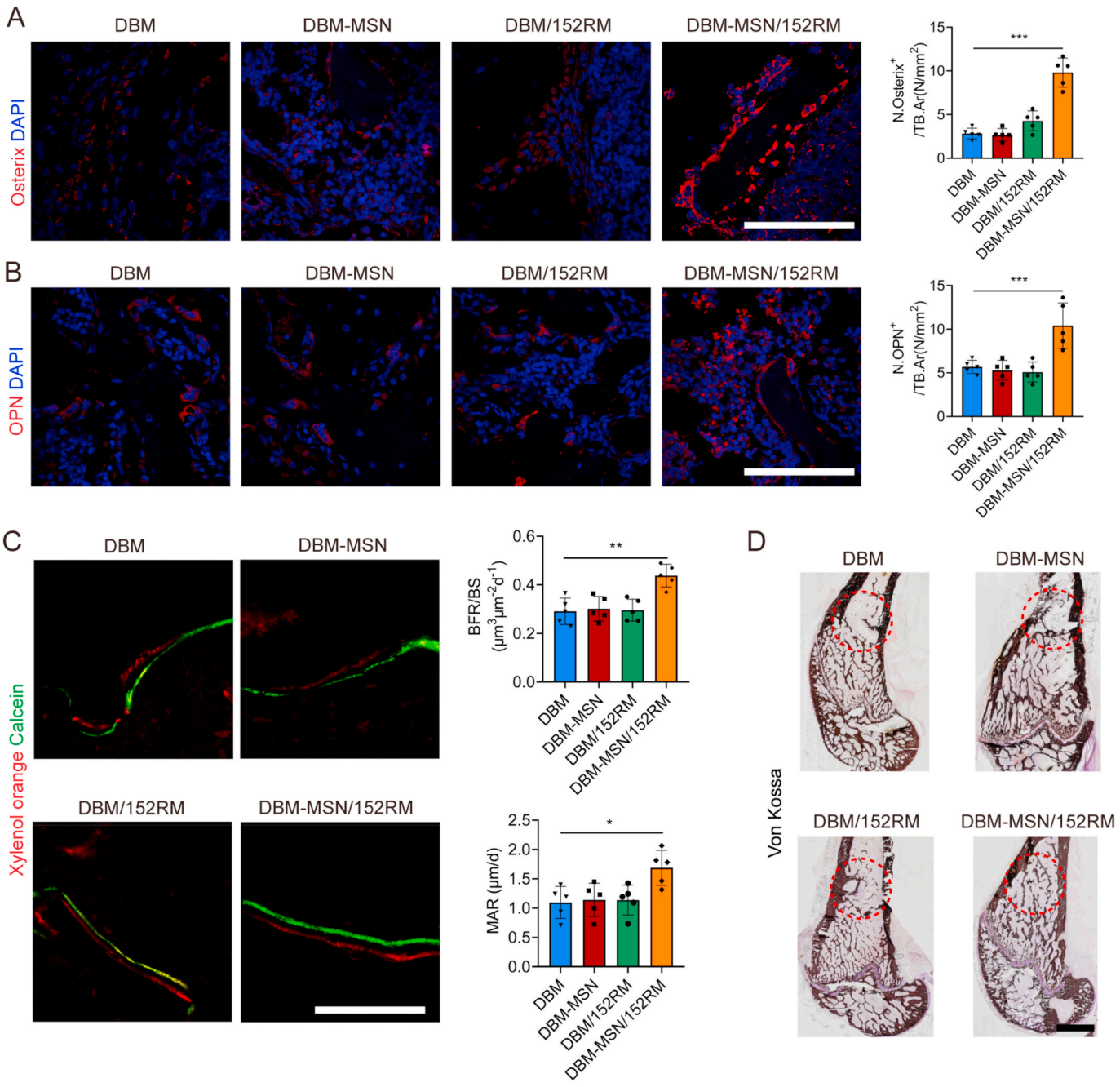

Fig. 10. DBM-MSN/152RM scaffolds promote bone formation and maturation *in vivo*. (A) Representative immunostaining images of osterix (red) in the BM 8 weeks after DBM, DBM-MSN, DBM/152RM and DBM-MSN/152RM scaffold implantation. (n = 5 rats per group). Scale bar, 100 μm. (B) Representative immunostaining images of osteopontin (red) in the BM 8 weeks after DBM, DBM-MSN, DBM/152RM and DBM-MSN/152RM scaffold implantation. (n = 5 rats per group). Scale bar, 100 μm. (C) Representative images of xylenol orange and calcein double labeling of new bone regeneration, quantification of mineral apposition rate (MAR) and bone formation rate (BFR) 4 weeks after DBM, DBM-MSN, DBM/152RM and DBM-MSN/152RM scaffold implantation (n = 5 rats per group). Scale bar, 20 μm. (D) Von Kossa staining images showing the mineralization of bone matrix 8 weeks after DBM, DBM-MSN, DBM/152RM and DBM-MSN/152RM scaffold implantation. (n = 5 rats per group). Scale bar, 50 μm. Data are shown as the mean ± SD. *P < 0.05, **P < 0.01, ***P < 0.001; ANOVA was employed. For all panels in this figure, data are representative of three independent experiments.

downregulates the activity of the ATF3 promoter, suggesting that ATF3 may be a downstream factor of Runx2 [52]. ATF3 is transcriptionally activated by the binding of β-catenin and TCF4 to the redundant TCF4 site in the proximal promoter region of the ATF3 gene, indicating that ATF3 is a direct target of the β-catenin pathway [54]. *In vivo* experiments also confirmed that 152RM promoted the formation and mineralization of new bone in the bone defects of DBM-MSN/152RM scaffolds. Thus, 152RM decreased ATF3 expression and activated the β-catenin pathway to induce osteogenic differentiation.

The formation of blood vessels influences the microenvironment of bone regeneration [22]. PTP1B is an important negative regulator of the VEGFR2 signaling pathway in endothelial cells [55]. Endothelium-specific deletion of PTP1B resulted in a VEGF-driven increase in ERK activation, which is critical to vessel formation [36]. Intriguingly, 152RM promotes EC migration by enhancing integrin αvβ3 and VEGFR2 signaling. There was a close cooperative binding interaction between integrin αvβ3 and VEGFR2 [56]. Integrin αvβ3 is one of the most critical factors for angiogenesis in the integrin family, and it not

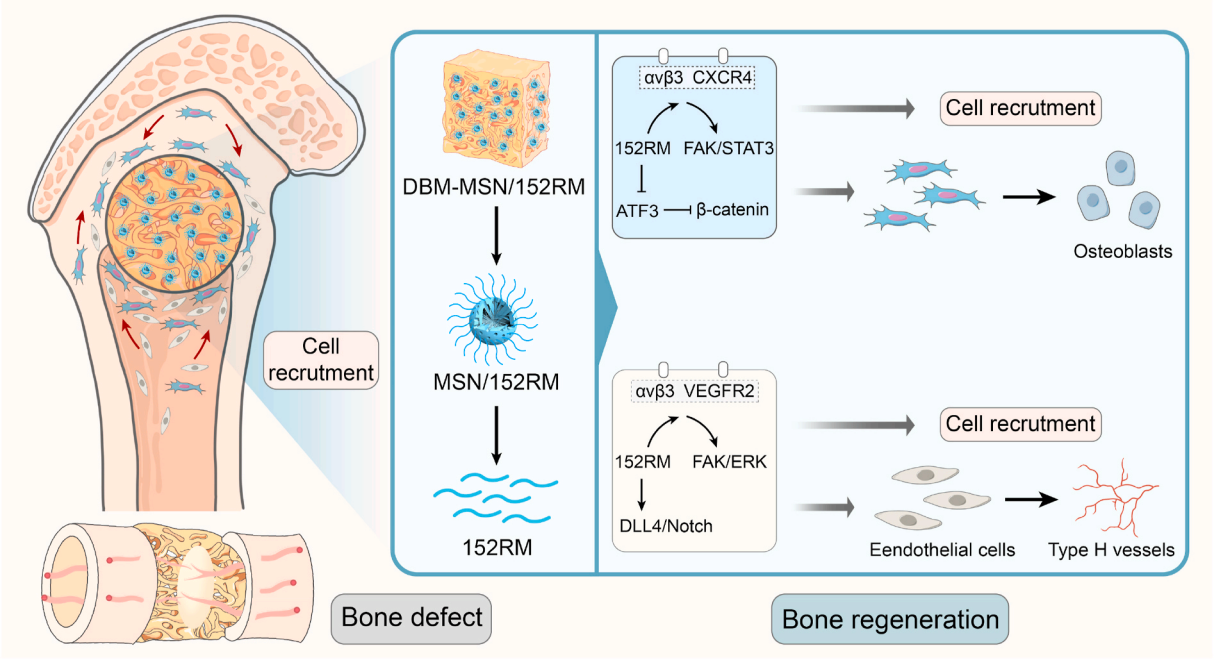

Fig. 11. Schematic illustration of the role of DBM-MSN/152RM scaffolds in promoting bone regeneration. During the repair of bone defects, 152RM promotes cell recruitment and osteogenic differentiation and induces the formation of $CD31^{hi}Emcn^{hi}$ vessels.

only promotes EC mobility but also enhances EC adhesion to scaffolds. In the present study, we confirmed that 152RM increases the basal level of VEGFR2 phosphorylation in ECs. These data are in line with a previous study showing that PTP1B inhibitors result in significant increases in VEGFR2-mediated EC functions [57]. FAK plays a key role in bridging integrin αvβ3 and VEGFR2, thereby activating downstream ERK1/2 expression [58]. As predicted, 152RM increased the phosphorylation levels of FAK and ERK1/2. *In vivo* experiments also confirmed that DBM-MSN/152RM scaffolds recruit a large number of ECs to bone defects. Furthermore, our data revealed that 152RM can stimulate MSCs to secrete VEGF, which may directly participate in EC migration and angiogenesis. It has been reported that VEGF derived from osteogenic progenitor cells could combine angiogenesis and osteogenesis in bone defect repair, regulate the process of intramembranous and endochondral ossification, and recruit osteoclasts to participate in bone reconstruction [59]. Thus, 152RM induces EC migration to bone defects, which is at least partly mediated by integrin αvβ3 and VEGFR2 signaling.

To date, some factors have been confirmed to induce the proliferation of ECs, vascular assembly and stabilization, such as PDGF-BB and slit guidance ligand 3 (SLIT3) [60,61]. ECs can secrete factors that promote vessel assembly and stabilization and promote bone formation, such as hypoxia-inducible factor 1 alpha (HIF-1α), Notch, and VEGF [62,63]. Recently, a subtype of capillary termed type H vessels was associated with bone formation, which is characterized by high expression of CD31 and endomucin ($CD31^{hi}Emcn^{hi}$) [22,63]. Additionally, PTP1B is an important negative regulator of the PDGFRβ signaling pathway, which regulates the type H endothelium in a manner interdependent with the Notch and Hif-1α signaling cascades in ECs [63]. [51]. Notch and its ligand delta-like 4 transduce signaling via cell–cell contact between ECs. The overactivation of Notch signaling in ECs is related to increases in angiogenesis and osteogenesis [62]. In this study, 152RM released from DBM-MSN/152RM scaffolds promoted the formation of $CD31^{hi}Emcn^{hi}$ vessels *in vivo*. Importantly, we confirmed via *in vitro* and *in vivo* experiments that the Notch signaling pathway was activated by 152RM. On the other hand, EC-derived noggin stimulates osteogenic differentiation and chondrocyte hypertrophy in MSCs [64]. Therefore, 152RM regulates endothelial cell-specific and cell-autonomous Notch activity to couple bone angiogenesis with osteogenesis.

5. Conclusion

Our findings confirm the key role of inhibition of PTP1B Y152 phosphorylation in bone regeneration. In addition, DBM-MSN/152RM scaffolds have a strong capacity to recruit MSCs and ECs, which provides a novel perspective for the treatment of large bone defects. Therefore, 152RM may be a new target for the development of new osteogenic drugs for skeletal diseases in the future.

Authors' contributions

Y. Tang, K. Luo and Y. Chen designed and performed the research, analyzed data, and wrote the manuscript; Y. Chen, C. Chen, and J. Tan performed some experiments and analyzed the data; M. Deng and Q. Dai contributed to the animal experiments; X. Yu, and J. Liu performed some of the *in vitro* experiments; R. Zhou, C. Zhang and W. Wu participated in some of the *in vivo* experiments; S. Dong, J. Xu and F. Luo participated in designing the experiments; J. Xu, S. Dong and F. Luo supervised the study and revised the manuscript.

Declaration of competing interest

All the authors declare that they have no potential conflicts of interest.

Acknowledgements

This work was supported by grants from the National Natural Science Foundation of China (81974336 and 82002308). We would like to thank AJE (American Journal Experts) for English language editing.

Appendix A. Supplementary data

Supplementary data to this article can be found online at https://doi.org/10.1016/j.bioactmat.2020.12.025.

References

[1] J.D. Thomas, J.L. Kehoe, Bone Nonunion, StatPearls, Treasure, Island (FL), 2020.
[2] L.C. Ortinau, H. Wang, K. Lei, L. Deveza, Y. Jeong, Y. Hara, I. Grafe, S.B. Rosenfeld, D. Lee, B. Lee, D.T. Scadden, D. Park, Identification of functionally distinct Mx1+ alphaSMA+ periosteal skeletal stem cells, Cell Stem Cell 25 (6) (2019) 784–796, e5.
[3] A.D. Kurenkova, E.V. Medvedeva, P.T. Newton, A.S. Chagin, Niches for skeletal stem cells of mesenchymal origin, Front Cell Dev Biol 8 (2020) 592.
[4] C. Maes, T. Kobayashi, M.K. Selig, S. Torrekens, S.I. Roth, S. Mackem, G. Carmeliet, H.M. Kronenberg, Osteoblast precursors, but not mature osteoblasts, move into developing and fractured bones along with invading blood vessels, Dev. Cell 19 (2) (2010) 329–344.
[5] R.J. Petrie, A.D. Doyle, K.M. Yamada, Random versus directionally persistent cell migration, Nat. Rev. Mol. Cell Biol. 10 (8) (2009) 538–549.
[6] T.J. Harris, U. Tepass, Adherens junctions: from molecules to morphogenesis, Nat. Rev. Mol. Cell Biol. 11 (7) (2010) 502–514.
[7] Y. Yan, H. Chen, H. Zhang, C. Guo, K. Yang, K. Chen, R. Cheng, N. Qian, N. Sandler, Y.S. Zhang, H. Shen, J. Qi, W. Cui, L. Deng, Vascularized 3D printed scaffolds for promoting bone regeneration, Biomaterials 190–191 (2019) 97–110.
[8] L.H. Wong, E.R. Eden, C.E. Futter, Roles for ER:endosome membrane contact sites in ligand-stimulated intraluminal vesicle formation, Biochem. Soc. Trans. 46 (5) (2018) 1055–1062.
[9] C.O. Arregui, A. Gonzalez, J.E. Burdisso, A.E. Gonzalez Wusener, Protein tyrosine phosphatase PTP1B in cell adhesion and migration, Cell Adhes. Migrat. 7 (5) (2013) 418–423.
[10] Y. Wang, F. Yan, Q. Ye, X. Wu, F. Jiang, PTP1B inhibitor promotes endothelial cell motility by activating the DOCK180/Rac1 pathway, Sci. Rep. 6 (2016) 24111.
[11] M.V. Hernandez, D.P. Wehrendt, C.O. Arregui, The protein tyrosine phosphatase PTP1B is required for efficient delivery of N-cadherin to the cell surface, Mol. Biol. Cell 21 (8) (2010) 1387–1397.
[12] K. Luo, Y. Tang, X. Gao, J. Tan, B. Yu, J. Xu, F. Luo, Inhibition of protein-tyrosine phosphatase 1B phosphorylation enhances early adhesion of mesenchymal stem cells to facilitate fabrication of tissue-engineered bone, J Tissue Eng Regen Med 14 (4) (2020) 575–587.
[13] H. Liu, M. Lin, X. Liu, Y. Zhang, Y. Luo, Y. Pang, H. Chen, D. Zhu, X. Zhong, S. Ma, Y. Zhao, Q. Yang, X. Zhang, Doping bioactive elements into a collagen scaffold based on synchronous self-assembly/mineralization for bone tissue engineering, Bioact Mater 5 (4) (2020) 844–858.
[14] H. Zhang, L. Yang, X.G. Yang, F. Wang, J.T. Feng, K.C. Hua, Q. Li, Y.C. Hu, Demineralized bone matrix carriers and their clinical applications: an overview, Orthop. Surg. 11 (5) (2019) 725–737.
[15] C. Yao, W. Wu, H. Tang, X. Jia, J. Tang, X. Ruan, F. Li, D.T. Leong, D. Luo, D. Yang, Self-assembly of stem cell membrane-camouflaged nanocomplex for microRNA-mediated repair of myocardial infarction injury, Biomaterials 257 (2020) 120256.
[16] X. Hong, X. Zhong, G. Du, Y. Hou, Y. Zhang, Z. Zhang, T. Gong, L. Zhang, X. Sun, The pore size of mesoporous silica nanoparticles regulates their antigen delivery efficiency, Sci Adv 6 (25) (2020) eaaz4462.
[17] B.M. Abdallah, H.M. Khattab, Recent approaches for isolating and culturing mouse bone marrow-derived mesenchymal stromal stem cells, Curr. Stem Cell Res. Ther. 15 (1) (2020).
[18] Y.N. Yang, S. Bernardi, H. Song, J. Zhang, M.H. Yu, J.C. Reid, E. Strounina, D. J. Searles, C.Z. Yu, Anion assisted synthesis of large pore hollow dendritic mesoporous organosilica nanoparticles: understanding the composition gradient, Chem. Mater. 28 (3) (2016) 704–707.
[19] G. Zhao, Y. Chen, Y. He, F. Chen, Y. Gong, S. Chen, Y. Xu, Y. Su, C. Wang, J. Wang, Succinylated casein-coated peptide-mesoporous silica nanoparticles as an antibiotic against intestinal bacterial infection, Biomater Sci 7 (6) (2019) 2440–2451.
[20] K.R. Rhodes, R.A. Meyer, J. Wang, S.Y. Tzeng, J.J. Green, Biomimetic tolerogenic artificial antigen presenting cells for regulatory T cell induction, Acta Biomater. 112 (2020) 136–148.
[21] T. Dong, C. Duan, S. Wang, X. Gao, Q. Yang, W. Yang, Y. Deng, Multifunctional surface with enhanced angiogenesis for improving long-term osteogenic fixation of poly(ether ether ketone) implants, ACS Appl. Mater. Interfaces 12 (13) (2020) 14971–14982.
[22] Y. Tang, M. Hu, Y. Xu, F. Chen, S. Chen, M. Chen, Y. Qi, M. Shen, C. Wang, Y. Lu, Z. Zhang, H. Zeng, Y. Quan, F. Wang, Y. Su, D. Zeng, S. Wang, J. Wang, Megakaryocytes promote bone formation through coupling osteogenesis with angiogenesis by secreting TGF-beta1, Theranostics 10 (5) (2020) 2229–2242.
[23] C. Dou, N. Ding, F. Luo, T. Hou, Z. Cao, Y. Bai, C. Liu, J. Xu, S. Dong, Graphene-based MicroRNA transfection blocks preosteoclast fusion to increase bone formation and vascularization, Adv. Sci. 5 (2) (2018) 1700578.
[24] L. Wang, S. He, X. Wu, S. Liang, Z. Mu, J. Wei, F. Deng, Y. Deng, S. Wei, Polyetheretherketone/nano-fluorohydroxyapatite composite with antimicrobial activity and osseointegration properties, Biomaterials 35 (25) (2014) 6758–6775.
[25] L. Qin, L. Hung, K. Leung, X. Guo, S. Bumrerraj, L. Katz, Staining intensity of individual osteons correlated with elastic properties and degrees of mineralization, J. Bone Miner. Metabol. 19 (6) (2001) 359–364.
[26] C.L. Duvall, W.R. Taylor, D. Weiss, R.E. Guldberg, Quantitative microcomputed tomography analysis of collateral vessel development after ischemic injury, Am. J. Physiol. Heart Circ. Physiol. 287 (1) (2004) H302–H310.
[27] Y. Wang, C. Wan, L. Deng, X. Liu, X. Cao, S.R. Gilbert, M.L. Bouxsein, M.C. Faugere, R.E. Guldberg, L.C. Gerstenfeld, V.H. Haase, R.S. Johnson, E. Schipani, T. L. Clemens, The hypoxia-inducible factor alpha pathway couples angiogenesis to osteogenesis during skeletal development, J. Clin. Invest. 117 (6) (2007) 1616–1626.
[28] L. Xian, X. Wu, L. Pang, M. Lou, C.J. Rosen, T. Qiu, J. Crane, F. Frassica, L. Zhang, J.P. Rodriguez, J. Xiaofeng, Y. Shoshana, X. Shouhong, E. Argiris, W. Mei, C. Xu, Matrix IGF-1 maintains bone mass by activation of mTOR in mesenchymal stem cells, Nat. Med. 18 (7) (2012) 1095–1101.
[29] G. Zhen, C. Wen, X. Jia, Y. Li, J.L. Crane, S.C. Mears, F.B. Askin, F.J. Frassica, W. Chang, J. Yao, J.A. Carrino, A. Cosgarea, D. Artemov, Q. Chen, Z. Zhao, X. Zhou, L. Riley, P. Sponseller, M. Wan, W.W. Lu, X. Cao, Inhibition of TGF-beta signaling in mesenchymal stem cells of subchondral bone attenuates osteoarthritis, Nat. Med. 19 (6) (2013) 704–712.
[30] S.M. Bittner, B.T. Smith, L. Diaz-Gomez, C.D. Hudgins, A.J. Melchiorri, D.W. Scott, J.P. Fisher, A.G. Mikos, Fabrication and mechanical characterization of 3D printed vertical uniform and gradient scaffolds for bone and osteochondral tissue engineering, Acta Biomater. 90 (2019) 37–48.
[31] W.G. Cui, X.H. Li, C.Y. Xie, J.G. Chen, J.E. Zou, S.B. Zhou, J.E. Weng, Controllable growth of hydroxyapatite on electrospun poly(DL-lactide) fibers grafted with chitosan as potential tissue engineering scaffolds, Polymer 51 (11) (2010) 2320–2328.
[32] Q. Yu, Y. Han, T. Tian, Q. Zhou, Z. Yi, J. Chang, C. Wu, Chinese sesame stick-inspired nano-fibrous scaffolds for tumor therapy and skin tissue reconstruction, Biomaterials 194 (2019) 25–35.
[33] M. Laurenti, A. Lamberti, G.G. Genchi, I. Roppolo, G. Canavese, C. Vitale-Brovarone, G. Ciofani, V. Cauda, Graphene oxide finely tunes the bioactivity and drug delivery of mesoporous ZnO scaffolds, ACS Appl. Mater. Interfaces 11 (1) (2019) 449–456.
[34] I. Acebron, R.D. Righetto, C. Schoenherr, S. de Buhr, P. Redondo, J. Culley, C. F. Rodriguez, C. Daday, N. Biyani, O. Llorca, A. Byron, M. Chami, F. Grater, J. Boskovic, M.C. Frame, H. Stahlberg, D. Lietha, Structural basis of Focal Adhesion Kinase activation on lipid membranes, EMBO J. 39 (19) (2020), e104743.
[35] H. Sha, D. Zhang, Y. Zhang, Y. Wen, Y. Wang, ATF3 promotes migration and M1/M2 polarization of macrophages by activating tenascinC via Wnt/betacatenin pathway, Mol. Med. Rep. 16 (3) (2017) 3641–3647.
[36] A.A. Lanahan, D. Lech, A. Dubrac, J. Zhang, Z.W. Zhuang, A. Eichmann, M. Simons, PTP1b is a physiologic regulator of vascular endothelial growth factor signaling in endothelial cells, Circulation 130 (11) (2014) 902–909.
[37] A. Sundararaman, Y. Fukushima, J.C. Norman, A. Uemura, H. Mellor, RhoJ regulates alpha5beta1 integrin trafficking to control fibronectin remodeling during angiogenesis, Curr. Biol. 30 (11) (2020) 2146–2155, e5.
[38] X. Zhao, J.L. Guan, Focal adhesion kinase and its signaling pathways in cell migration and angiogenesis, Adv. Drug Deliv. Rev. 63 (8) (2011) 610–615.
[39] D. Zhao, T. Zhu, J. Li, L. Cui, Z. Zhang, X. Zhuang, J. Ding, Poly(lactic-co-glycolic acid)-based composite bone-substitute materials, Bioact Mater 6 (2) (2021) 346–360.
[40] Y. Chen, K. Lee, N. Kawazoe, Y. Yang, G. Chen, ECM scaffolds mimicking extracellular matrices of endochondral ossification for the regulation of mesenchymal stem cell differentiation, Acta Biomater. 114 (2020) 158–169.
[41] H.S. Kim, N. Mandakhbayar, H.W. Kim, K.W. Leong, H.S. Yoo, Protein-reactive Nanofibrils Decorated with Cartilage-Derived Decellularized Extracellular Matrix for Osteochondral Defects, Biomaterials, 2020, p. 120214.
[42] S.B. Goodman, T. Lin, Modifying MSC phenotype to facilitate bone healing: biological approaches, Front Bioeng Biotechnol 8 (2020) 641.
[43] J.E. Burdisso, A. Gonzalez, C.O. Arregui, PTP1B promotes focal complex maturation, lamellar persistence and directional migration, J. Cell Sci. 126 (Pt 8) (2013) 1820–1831.
[44] K. Luo, X. Gao, Y. Gao, Y. Li, M. Deng, J. Tan, J. Gou, C. Liu, C. Dou, Z. Li, Z. Zhang, J. Xu, F. Luo, Multiple integrin ligands provide a highly adhesive and osteoinductive surface that improves selective cell retention technology, Acta Biomater. 85 (2019) 106–116.
[45] M. Fujita, P. Davari, Y.K. Takada, Y. Takada, Stromal cell-derived factor-1 (CXCL12) activates integrins by direct binding to an allosteric ligand-binding site (site 2) of integrins without CXCR4, Biochem. J. 475 (4) (2018) 723–732.
[46] J. Cui, C. Shu, J. Xu, D. Chen, J. Li, K. Ding, M. Chen, A. Li, J. He, Y. Shu, L. Yang, R. Zhang, J. Zhou, JP1 suppresses proliferation and metastasis of melanoma through MEK1/2 mediated NEDD4L-SP1-Integrin alphavbeta3 signaling, Theranostics 10 (18) (2020) 8036–8050.
[47] A. Blazquez-Prunera, C.R. Almeida, M.A. Barbosa, Fibroblast growth factor improves the motility of human mesenchymal stem cells expanded in a human plasma-derived xeno-free medium through alphaVbeta3 integrin, J Tissue Eng Regen Med 13 (1) (2019) 36–45.
[48] H. Liu, H. Peng, Y. Wu, C. Zhang, Y. Cai, G. Xu, Q. Li, X. Chen, J. Ji, Y. Zhang, H. W. OuYang, The promotion of bone regeneration by nanofibrous hydroxyapatite/chitosan scaffolds by effects on integrin-BMP/Smad signaling pathway in BMSCs, Biomaterials 34 (18) (2013) 4404–4417.
[49] D. Liu, X. Kou, C. Chen, S. Liu, Y. Liu, W. Yu, T. Yu, R. Yang, R. Wang, Y. Zhou, S. Shi, Circulating apoptotic bodies maintain mesenchymal stem cell homeostasis and ameliorate osteopenia via transferring multiple cellular factors, Cell Res. 28 (9) (2018) 918–933.
[50] L. Song, F. Zhang, R. Zhou, J. Xiao, L. He, F. Dai, hCTLA4-Gene-Modified human bone marrow-derived mesenchymal stem cells (hBMMSCs) maintain POSTN secretion to enhance the migration capability of allogeneic hBMMSCs through the integrin alphavbeta3/FAK/ERK signaling pathway, Stem Cell. Int. 2020 (2020) 3608284.
[51] Z.W. Zheng, Y.H. Chen, D.Y. Wu, J.B. Wang, M.M. Lv, X.S. Wang, J. Sun, Z. Y. Zhang, Development of an accurate and proactive immunomodulatory strategy

to improve bone substitute material-mediated osteogenesis and angiogenesis, Theranostics 8 (19) (2018) 5482–5500.
[52] B.C. Jeong, ATF3 mediates the inhibitory action of TNF-alpha on osteoblast differentiation through the JNK signaling pathway, Biochem. Biophys. Res. Commun. 499 (3) (2018) 696–701.
[53] J.K. Park, H. Jang, S. Hwang, E.J. Kim, D.E. Kim, K.B. Oh, D.J. Kwon, J.T. Koh, K. Kimura, H. Inoue, W.G. Jang, J.W. Lee, ER stress-inducible ATF3 suppresses BMP2-induced ALP expression and activation in MC3T3-E1 cells, Biochem. Biophys. Res. Commun. 443 (1) (2014) 333–338.
[54] M. Inoue, Y. Uchida, M. Edagawa, M. Hirata, J. Mitamura, D. Miyamoto, K. Taketani, S. Sekine, J. Kawauchi, S. Kitajima, The stress response gene ATF3 is a direct target of the Wnt/beta-catenin pathway and inhibits the invasion and migration of HCT116 human colorectal cancer cells, PLoS One 13 (7) (2018), e0194160.
[55] Y. Wang, F. Yan, W. Zhang, S. Pang, F. Jiang, Inhibiting protein tyrosine phosphatase 1B to improve regenerative functions of endothelial cells, J. Cardiovasc. Pharmacol. 71 (2) (2018) 59–64.
[56] J. Wu, T.L. Strawn, M. Luo, L. Wang, R. Li, M. Ren, J. Xia, Z. Zhang, W. Ma, T. Luo, D.A. Lawrence, W.P. Fay, Plasminogen activator inhibitor-1 inhibits angiogenic signaling by uncoupling vascular endothelial growth factor receptor-2-alphaVbeta3 integrin cross talk, Arterioscler. Thromb. Vasc. Biol. 35 (1) (2015) 111–120.
[57] F. Yan, Y. Wang, X. Wu, H.M. Peshavariya, G.J. Dusting, M. Zhang, F. Jiang, Nox4 and redox signaling mediate TGF-beta-induced endothelial cell apoptosis and phenotypic switch, Cell Death Dis. 5 (2014), e1010.
[58] T.M. Danilucci, P.K. Santos, B.C. Pachane, G.F.D. Pisani, R.L.B. Lino, B.C. Casali, W.F. Altei, H.S. Selistre-de-Araujo, Recombinant RGD-disintegrin DisBa-01 blocks integrin alphavbeta3 and impairs VEGF signaling in endothelial cells, Cell Commun. Signal. 17 (1) (2019) 27.
[59] K. Hu, B.R. Olsen, Osteoblast-derived VEGF regulates osteoblast differentiation and bone formation during bone repair, J. Clin. Invest. 126 (2) (2016) 509–526.
[60] R. Xu, A. Yallowitz, A. Qin, Z. Wu, D.Y. Shin, J.M. Kim, S. Debnath, G. Ji, M. P. Bostrom, X. Yang, C. Zhang, H. Dong, P. Kermani, S. Lalani, N. Li, Y. Liu, M. G. Poulos, A. Wach, Y. Zhang, K. Inoue, A. Di Lorenzo, B. Zhao, J.M. Butler, J. H. Shim, L.H. Glimcher, M.B. Greenblatt, Targeting skeletal endothelium to ameliorate bone loss, Nat. Med. 24 (6) (2018) 823–833.
[61] H. Xie, Z. Cui, L. Wang, Z. Xia, Y. Hu, L. Xian, C. Li, L. Xie, J. Crane, M. Wan, G. Zhen, Q. Bian, B. Yu, W. Chang, T. Qiu, M. Pickarski, L.T. Duong, J.J. Windle, X. Luo, E. Liao, X. Cao, PDGF-BB secreted by preosteoclasts induces angiogenesis during coupling with osteogenesis, Nat. Med. 20 (11) (2014) 1270–1278.
[62] S.K. Ramasamy, A.P. Kusumbe, L. Wang, R.H. Adams, Endothelial Notch activity promotes angiogenesis and osteogenesis in bone, Nature 507 (7492) (2014) 376–380.
[63] A.P. Kusumbe, S.K. Ramasamy, R.H. Adams, Coupling of angiogenesis and osteogenesis by a specific vessel subtype in bone, Nature 507 (7492) (2014) 323–328.
[64] M.N. Hsu, F.J. Yu, Y.H. Chang, K.L. Huang, N.N. Pham, V.A. Truong, M.W. Lin, N. T. Kieu Nguyen, S.M. Hwang, Y.C. Hu, CRISPR interference-mediated noggin knockdown promotes BMP2-induced osteogenesis and calvarial bone healing, Biomaterials 252 (2020) 120094.